DELIVERABLE REPORT

VALHALLA

Report on final new materials developed (perovskite and charge extraction layers)

Deliverable D1.2
JUNE-2025

PREPARED BY
IIT
COORDINATED BY
UVEG

Funded by
the European Union

VALHALLA is a 3-year research and innovation project funded by the European Commission through the Horizon Europe Research and Innovation Action (RIA) grant N°101082176, responding to the call for a "*Sustainable, secure and competitive energy supply*" (HORIZON-CL5-2021-D3-03).

VALHALLA aims to develop perovskite solar cells and modules with power conversion efficiencies above 26 % (modules > 23 %) and extrapolated operational lifetime > 25 years, following an eco-design approach: employing harmful-solvent-free perovskite deposition, optimized use of materials, circularity, recyclability, scalable and low-cost manufacturing processes, to create a viable economic pathway for the European commercialization of this sustainable technology.

VALHALLA is formed by a multi-disciplinary consortium: 12 partners from 8 European countries; 3 industrial partners & 9 RTOs, covering the whole value chain of innovation from research centres to technology providers, end-users and market and policies.

Project info	101082176 – VALHALLA – (HORIZON-CL5-2021-D3-03)
Deliverable Title	D1.2 : Report on final new materials developed (perovskite and charge extraction layers)
Lead Beneficiary	Istituto Italiano di Tecnologia
Authors	Annamaria Petrozza, Davide Regaldo, Henry Snaith, Tadas Malinauskas, Javier Sebastian, Maria Monrabal, Michele Sessolo, Daniele Meggiolaro
Approved by	Henk Bolink
Dissemination level	Public
Due date	30th June 2025
Submission date	2nd of July 2025
Version	2
Linked to WP - task	WP1 – all tasks

Funded by the European Union

This project has received funding from the European Union's Horizon Europe research and innovation programme under grant agreement No. 101082176

VALHALLA Consortium

Organization name	Short name	Country
UNIVERSITAT DE VALENCIA	UVEG	ES
KAUNO TECHNOLOGIJOS UNIVERSITETAS	KTU	LT
RIJKSUNIVERSITEIT GRONINGEN	RUG	NL
CONSIGLIO NAZIONALE DELLE RICERCHE	CNR	IT
FONDAZIONE ISTITUTO ITALIANO DI TECNOLOGIA	IIT	IT
UNIVERSITE DE LIEGE	ULiège	BE
THE CHANCELLOR, MASTERS AND SCHOLARS OF THE UNIVERSITY OF OXFORD	UOXF	UK
3SUN SRL	3SUN	IT
TEKNOLOGIAN TUTKIMUSKESKUS VTT OY	VTT	FI
ICARES CONSULTING/BECQUEREL INSTITUTE FRANCE	BI/BI F	BE/FR
ARK METRICA LTD	ARKM	UK
CSEM CENTRE SUISSE D'ELECTRONIQUE ET DE MICROTECHNIQUE SA - RECHERCHE ET DEVELOPPEMENT	CSEM	CH

Disclaimer
Funded by the European Union. Views and opinions expressed are however those of the author(s) only and do not necessarily reflect those of the European Union or CINEA. Neither the European Union nor the granting authority can be held responsible for them.

How to Cite
Annamaria Petrozza, Davide Regaldo, Henry Snaith, Tadas Malinauskas, Javier Sebastian, Maria Monrabal, Michele Sessolo, Daniele Meggiolaro (2025). Deliverable 1.2 Report: Report on final new materials developed (perovskite and charge extraction layers). in Project VALHALLA: Perovskite Solar Cells with Enhanced Stability and Applicability (No. 101082176). European Union. PUBLIC [Communicate on 02/07/2025].

Table of Content

Funded by the European Union
This project has received funding from the European Union's Horizon Europe research and innovation programme under grant agreement No. 101082176

List of Tables

List of Figures

Funded by the European Union
This project has received funding from the European Union's Horizon Europe research and innovation programme under grant agreement No. 101082176

Funded by the European Union

This project has received funding from the European Union's Horizon Europe research and innovation programme under grant agreement No. 101082176

Abbreviations and acronyms list

Abbreviation	Meaning	Abbreviation	Meaning
AFM	Atomic Force Microscopy	ALD	Atomic Layer Deposition
AZO	Aluminum Zinc Oxide	CBM	Conduction Band Minimum
CNR	Consiglio Nazionale delle Ricerche	CSEM	Centre Suisse d'Électronique et de Microtechnique
DFE	Defect Formation Energy	DMF	Dimethylformamide
DMA	Dimethylammonium	DSC	Differential Scanning Calorimetry
ETL	Electron Transport Layer	FA	Formamidinium
FAI	Formamidinium Iodide	HTM	Hole Transport Material
ITO	Indium Tin Oxide	MA	Methylammonium
MAI	Methylammonium Iodide	MAPbI3	Methylammonium Lead Iodide
MAPI	Methylammonium Lead Iodide (alternate acronym)	NDI	Naphthalene Diimide
NMR	Nuclear Magnetic Resonance	PAAQ	Phenyl-Anthraquinone derivative
PBE	Perdew–Burke–Ernzerhof (exchange-correlation functional in DFT)	PBE0-SOC	Hybrid PBE functional with spin-orbit coupling
PbI2	Lead Iodide	PDMS	Polydimethylsiloxane
PERNI	Perinone-based electron-collecting molecule	PL	Photoluminescence
PLD	Pulsed Laser Deposition	PLQY	Photoluminescence Quantum Yield
PSC	Perovskite Solar Cell	QCM	Quartz Crystal Microbalance
RMS	Root Mean Square	SAM	Self-Assembled Monolayer
SEM	Scanning Electron Microscopy	SnO_2	Tin Oxide
SnOx	Non-stoichiometric Tin Oxide	TCO	Transparent Conductive Oxide
TGA	Thermogravimetric Analysis	UPS	Ultraviolet Photoelectron Spectroscopy
UV-Vis	Ultraviolet-Visible Spectroscopy	UVEG	Universitat de Valencia
VBM	Valence Band Maximum	VTT	Teknologian tutkimuskeskus VTT Oy
WP	Work Package	XPS	X-ray Photoelectron Spectroscopy
XRD	X-ray Diffraction		

1. Executive Summary

1.1. Description of the deliverable content and purpose

The purpose of this deliverable is to report about the range of perovskite absorbers, with bandgaps > 1.7 eV, 1.5-1.7 eV and < 1.5 eV, developed within the VALHALLA project and the charge transport layers optimized for each bandgap.

Perovskite absorbers. The perovskite absorbers have been evaporated according to different protocols, i.e. through sequential deposition or co-evaporation, according to the chemical composition of the expected compound. In particular, for narrow bandgap semiconductors based on Sn and Sn-Pb metal cations, protocols for precursors co-evaporation have been developed (**Sec. 1.3**). For mid-gap semiconductors a sequential deposition protocol has been developed for single A-site cation

Funded by the European Union
This project has received funding from the European Union's Horizon Europe research and innovation programme under grant agreement No. 101082176

perovskite (MA^+) (**Sec. 1.4.1)**, and for mixed Cs-FA cation (**Sec. 1.4.5**), while co-evaporation protocols have been developed for mix-cations compositions and in presence of additives acting as crystallization seeds (**Sec. 1.4.2** to **Sec. 1.4.5**). Then, for wide bandgap semiconductors a sequential deposition method has been developed for mix A-site cations pristine perovskites (**Sec. 1.5.1**) and a co-evaporation protocol has been developed for purely inorganic perovskites including passivating organic and inorganic additives (**Sec. 1.5.2**).

Organic charge transport materials. Derivatives of carbazole, phenothiazine, phenoxazine, triphenylethylene were synthesized for application in hole selective layers and basic characterization was done. Crosslinkable hole transporting material and procedure for their low temperature crosslinking in the layer were developed. Molecules were selected based on the feedback obtained from thermal, optical, electrochemical characterization and from the feedback obtained by their testing in devices. Overall, 38 goal materials were synthesized, characterized and evaluated for suitability of further testing, out of them 25 were selected and sent to the project partners for testing in PSCs. After evaluating investigated characteristics, ease of synthesis and potential for scale up from more than thirty compounds synthesized we have selected twenty five which best fitted the selection criteria for application in the perovskite solar cells. Below we list of selected representatives of the materials synthesized for the VALHALLA consortium. From the 1,4,5,8-naphthalene tetracarboxylic diimide derivatives compounds with best TGA profiles and suitable energy levels where chosen.

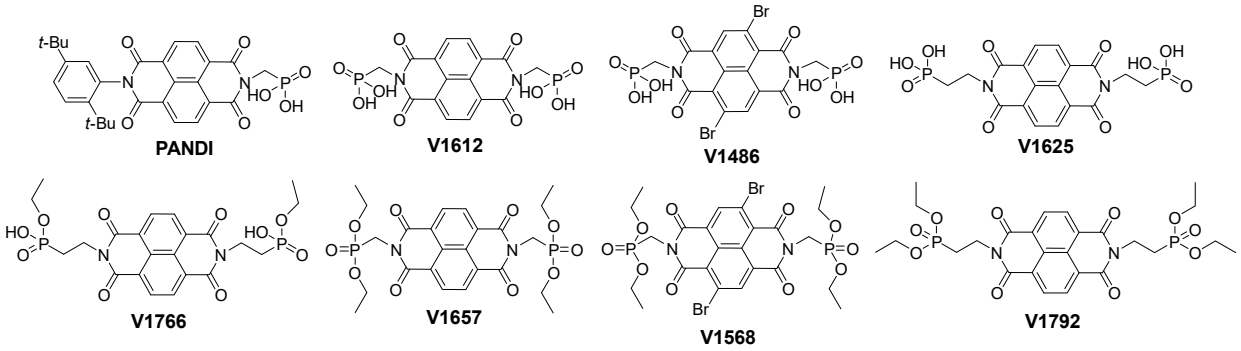

Figure 1 NDI materials selected for further testing in the devices

All selected NDI materials were of the symmetrical variety, this decision was governed by better characteristics as well as simpler, faster and more straightforward synthesis. Predominantly those are molecules with phosphonic acid functional groups, although after receiving feedback from partners some esters and partially hydrolized esters were also included.

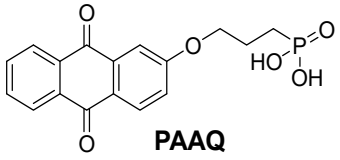

Figure 2 Anthraquinone material selected for further testing in the devices

Anthraquinone-based electron transporting material was also selected for further investigation, due to good performance in initial tests, energy levels were somewhat borderline, although TGA profile was good.

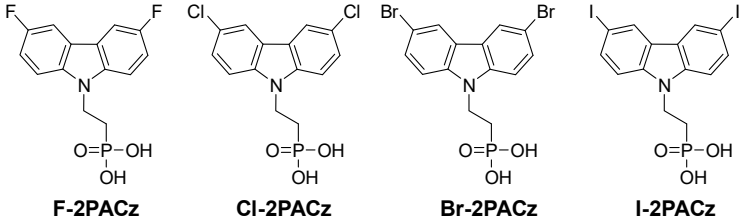

Funded by the European Union
This project has received funding from the European Union's Horizon Europe research and innovation programme under grant agreement No. 101082176

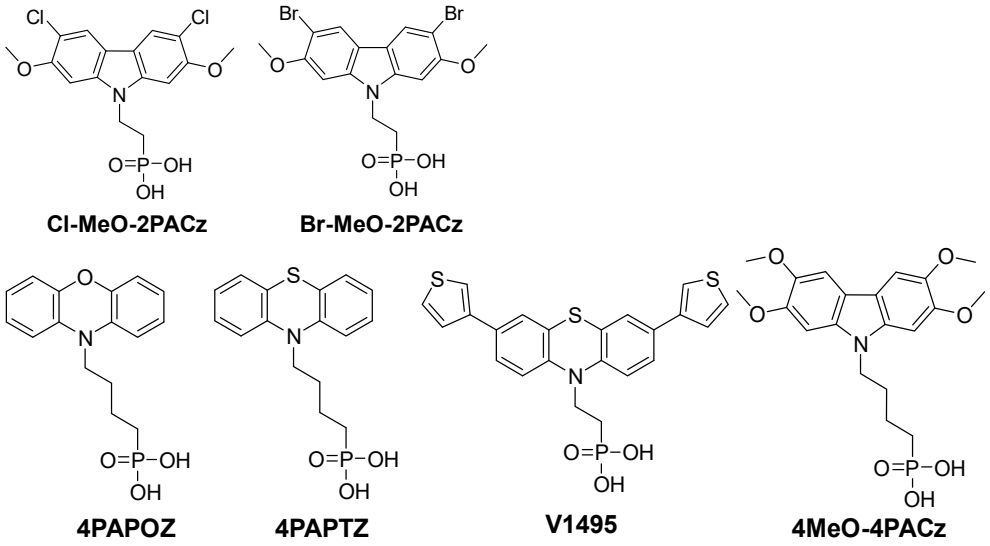

Figure 3 Hole selective materials selected for further testing in the devices

From the synthesized hole selective materials ones capable of forming self-assembling monolayers were the main focus of investigation. Specifically halogenated carbazole derivatives with deeper ionization energy levels, and molecules with atoms and functional groups providing additional interaction with perovskite layer.

Inorganic charge transport materials and electrodes. Pulsed laser deposition protocols have been developed for the growth of oxides and indium free electrodes.

1.2. Relation with other activities in the project

The content of this deliverable is related to work developed in WP1 for the achievement of the following objectives: **O1.1** develop metal halide perovskites with bandgaps <1.4, 1.5-1.7 and >1.7 with optimal optoelectronic figures of merit and stable; **O1.2** develop efficient charge transporting and charge recombination materials matching the energy levels of perovskite absorbers with different bandgaps; **O1.3 d**eliver solar cell materials and device stacks to WP2 and WP3 for subsequent device integration, encapsulation and module development; **O1.4** develop scalable and sustainable processing methods to minimize the environmental impact of perovskite PV.
The content of this deliverable is also strongly related to the activity of WP2 where devices are fabricated and the materials developed get assess and WP5 which focuses on the analysis of the whole life cycle (including recycling) of perovskite PV systems, thus including the materials synthesis.

Funded by the European Union
This project has received funding from the European Union's Horizon Europe research and innovation programme under grant agreement No. 101082176

2. Perovskite thin films with tuneable bandgap

This deliverable describes the perovskite materials developed during the project within WP1. We successfully grew polycrystalline perovskite films with low (<1.4 eV), intermediate (1.5-1.6 eV), and wide bandgap (>1.7 eV), serving the need for absorber layers for both single junction and tandem solar cells.

1.3. Low bandgap perovskite films

1.3.1. Co-evaporated $FASnI_3$ with bandgap of 1.4 eV

Among tin-based perovskites, $FASnI_3$ was selected due to the superior thermal stability of formamidinium (FA^+) cations compared to methylammonium (MA^+) cations. This stability is attributed to the higher evaporation rate and lower volatility of FA^+, as well as the tendency of MA^+ to fragment under heat. Furthermore, according to the state-of-the-art studies on solution-processed THPs have shown that the FASnI□ phase exhibits superior optoelectronic performance as solar cells.

The $FASnI_3$ films were prepared without any additives. High-purity precursors were thermally evaporated using two independent quartz crystal microbalances (QCMs) for real-time rate monitoring.

For comparison, $FASnI_3$ films were also fabricated using spin-coating. Co-evaporated films had a final thickness of approximately 400 nm (Figure 1a). Scanning electron microscopy (SEM) revealed a smooth surface morphology with uniform crystal domains of ~200 nm (Figure 1b). XRD confirmed that the co-evaporated $FASnI_3$ adopted a near-cubic phase with no detectable impurity phases, in contrast to the spin-coated films which showed additional phases (Figure 1c).

Optical characterization showed distinct differences between the two fabrication methods. Spin-coated films exhibited a broad absorption background in the long-wavelength region (~800 nm), indicating a higher density of tail states. This was consistent with the broad and blue-shifted photoluminescence (PL) observed (Figure 1d). In contrast, co-evaporated films displayed a sharper absorption edge, and a narrower PL peak centered near 950 nm, suggesting fewer mid-gap or tail states and reduced unintentional doping.

Chemical analysis via X-ray photoelectron spectroscopy (XPS) confirmed the dominant presence of Sn^{2+} in co-evaporated films (Figure 1f, g). This contrasts with spin-coated films using SnF□ additives, where surface oxidation is commonly observed. The absence of Sn^{4+} states imply minimal compensation from tin vacancies (V_{Sn}), which are known to increase hole concentrations in THPs. Finally, ultraviolet photoelectron spectroscopy (UPS) revealed that the Fermi level of the co-evaporated films is positioned near mid-gap (Figure 1h), further indicating intrinsic semiconductor behaviour and minimal p-type doping.

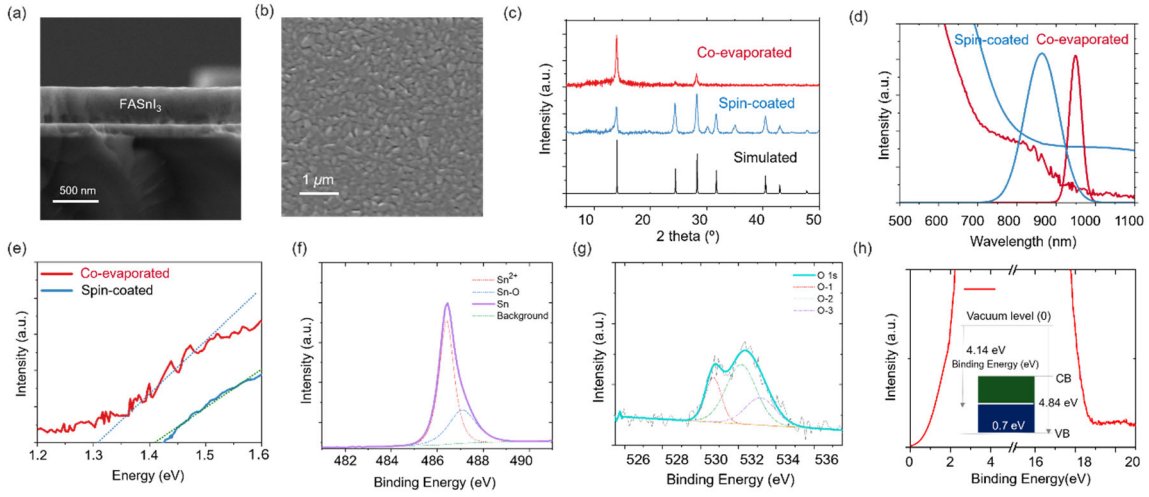

Figure 4: (a) Cross-section image of co-evaporated $FASnI_3$. (b) Surface image measured by SEM. (c) X-ray diffraction patterns of co-evaporated, spin-coated, and simulated $FASnI_3$ (d) Absorption and PL of co-evaporated and spin-coated $FASnI_3$ (e) Tauc analysis on co-evaporated and spin-coated $FASnI_3$ (f) Sn binding energy measure by XPS data. (g) Oxygen binding energy. (h) UPS spectra and simplied band structure.

Photo-stability of thin film of FASnI3 was directly compared with spin-coated FASnI3. The films were

Funded by the European Union
This project has received funding from the European Union's Horizon Europe research and innovation programme under grant agreement No. 101082176

annealed for 20 minutes at 120°C). All films were encapsulated in N2 filled glovebox and the photo-stability test was conducted in specially designed photo-aging chamber with N2 flowing. In Figure 5**a** photoluminescence with remarkably smaller full width half maximum compared to spin-coated FASnI3 implying less gap state densities. Smaller Urbach energy and Moss-Burstein effect was also observed in absorption of co-evaporated film compared to spin-coated film. After 48 hours of photodegradation, the PL peak of co-evaporated film showed slightly blue shifted and multiple impurity peaks generated. Meanwhile, PL peak of spin-coated film became much wider, and blue shifted to higher energy compared to co-evaporated film implying generation of defects and much severe Moss-Burstein effect making film highly p-doped. (Figure 5b-c) Urbach energy change were also more dramatic in spin coated film after 48 hours of photodegradation. Especially X-ray diffraction peaks were shifted to lower angle while insignificant change observed in co-evaporated film (Figure 5**f**).

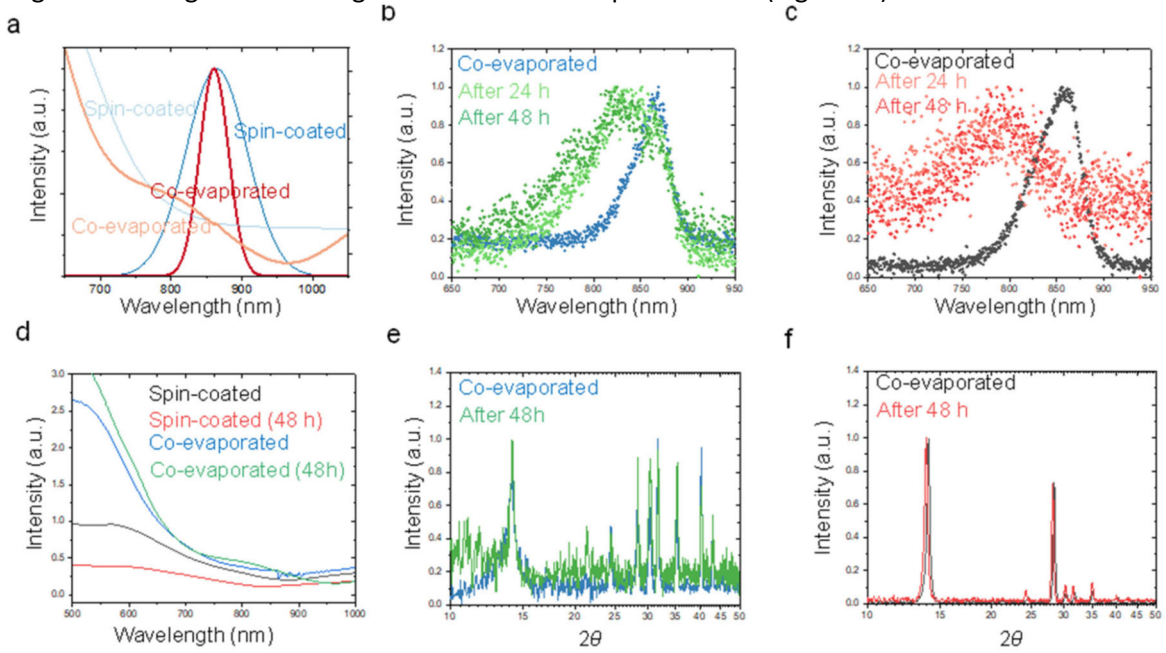

Figure 5: a) Photoluminescence and absorption of spin-coated and co-evaporated FASnI3 film, b) Photoluminescence spectra change of co-evaporated FASnI3 after 48 hours, c) Photoluminescence spectra change of spin-coated FASnI3 after 48 hours, d) Absorption change of spin coated/co-evaporated FASnI3 after 48 hours, e) X-ray diffraction pattern changes of coevaporated FASnI3 after 48 hours, f) X-ray diffraction pattern changes of spin-coated FASnI3 after 48 hours.

1.3.2. Co-evaporated mixed Sn-Pb perovskites (<1.3 eV bandgap)

UOXF developed mixed Sn-Pb perovskites by co-evaporation with the aim of achieving very low bandgap < 1.3 eV materials. The targeted stoichiometry was $CsFASn_{0.5}Pb_{0.5}I_3$, which should lead to the lowest bandgap among mixed Sn-Pb formulations. The co-evaporated perovskite films were compared to solution-processed ones, using nominally equal precursors stoichiometry, with a more established deposition process.

Funded by the European Union
This project has received funding from the European Union's Horizon Europe research and innovation programme under grant agreement No. 101082176

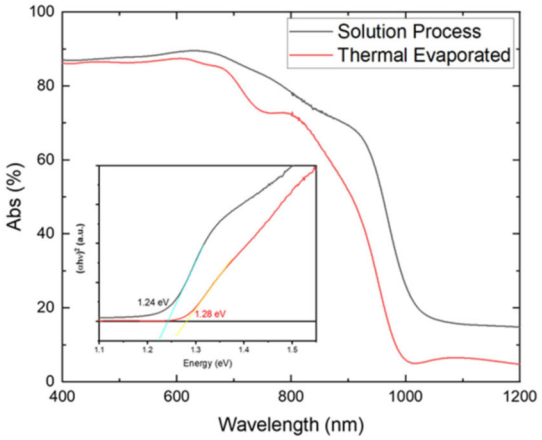

Figure 6: The optical aborption spectra of solution processed (spin coated) and vacuum processed (co-evaporated) Sn-Pb perovskite films (inset: Tauc plot).

The difference between the solution- and vacuum-processed Sn-Pb perovskite films can be observed by examining their optical properties. Figure 6 displays the absorbance spectra of solution spin-coated and co-evaporated Sn-Pb perovskite films. The spectra reveal that the vacuum processed perovskite film also has a sharp absorption edge like the solution processed films, implying good optoelectronic quality of the co-evaporated Sn-Pb perovskite layers. The absorption spectra of the thermally evaporated Sn-Pb perovskite films confirm a slightly wider bandgap of ≈ 1.28 eV compared to the solution processed Sn-Pb perovskite films, with a bandgap of 1.24 eV.

1.3.3. Other co-evaporated Sn/Pb perovskite films (1.3 eV bandgap)

Co-evaporated low bandgap perovskite films were also investigated at UVEG, using PbI_2, SnI_2 as the inorganic halide source and MAI as the A-cation. $MASn_xPb_{x-1}I_3$ vacuum-deposited thin films were prepared and Sn content x was varied from 0 ($MAPbI_3$) to 1 ($MASnI_3$), with x being 0, 0.2, 0.3, 0.5, 0.7, 0.8 and 1. The X-ray diffraction patterns of the whole series of film is reported in Figure 7a. The perovskite phase is obtained in all cases, although a reduction of the signal-to-noise ratio (SNR) is found for low Sn concentrations (20 to 50%) and for the pure Sn perovskite.

Funded by the European Union

This project has received funding from the European Union's Horizon Europe research and innovation programme under grant agreement No. 101082176

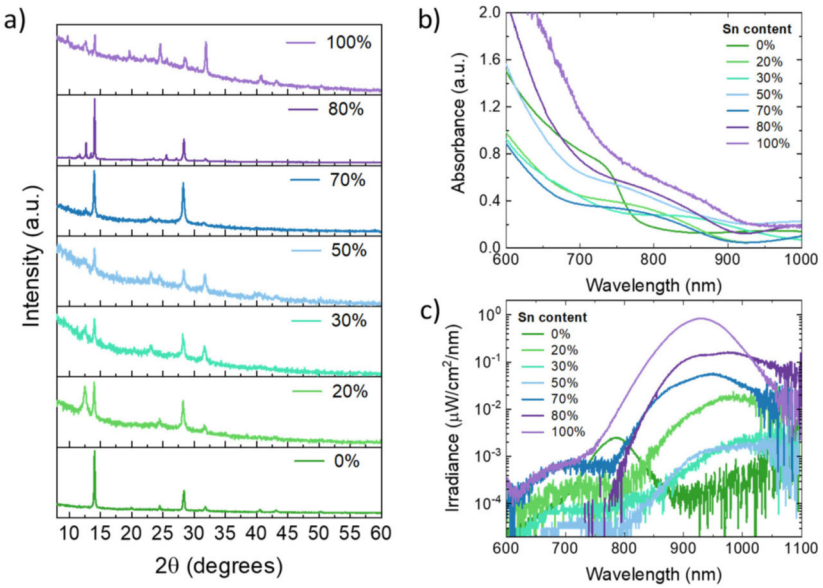

Figure 7: (a) X-ray diffraction patterns, b) absorbance and c) PL spectra of a series of $MASn_xPb_{x-1}I_3$ perovskite films as a function of Sn content.

A noticeable and expected red-shift in the absorption onset is observed when inserting and increasing the Sn content, as seen from the absorption spectra of the film series (Figure 7b). The formation of a Sn-based perovskites is also confirmed by a reduction of the absorption coefficient. The bandgap estimation is difficult due also to some scattering and interference in the high wavelength range, but it is at wavelength higher than 900 nm (1.38 eV) for most of the films. This is confirmed from PL measurements (Figure 7c), where PL maxima at about 950 nm (1.3 eV) are found for mixed Sn-Pb formulations.

1.4. Intermediate bandgap perovskite films (1.5-1.6 eV)

1.4.1. Sequentially evaporated $MAPbI_3$

UVEG has developed a reproducible protocol for sequential vacuum deposition of $MAPbI_3$ thin films. The sequential deposition process used in this work consists of two main steps. First, the inorganic precursor (PbI_2) is thermally evaporated onto the substrate under high vacuum conditions. In the second step, the organic precursor (MAI) is introduced, enabling the in situ conversion of the PbI_2 layer into the perovskite phase. A cross-sectional SEM image of a completed device (Figure 8C) reveals a perovskite film with a uniform thickness of approximately 370 nm and a columnar grain structure extending across the entire film thickness. The absence of voids or structural defects indicates high film quality and effective precursor conversion. A representative top-view SEM image shows surface grains with lateral dimensions exceeding 200 nm (Figure 8F), consistent with those observed in the cross-section. X-ray diffraction (XRD) analysis confirms the complete transformation of PbI_2 into the perovskite phase, evidenced by the absence of the characteristic PbI_2 peak at 12.5° and the presence of strong diffraction peaks corresponding to the perovskite structure (Figure 8A). UV-Vis absorption spectroscopy further supports this, showing a Sharp absorption Edge around 780 nm, typical of methylammonium lead iodide (MAPI) perovskites (Figure 8B). To assess the electronic quality of the films, steady-state photocarrier grating measurements were conducted, yielding an in-plane minority carrier diffusion length (L_d) of approximately 0.33 µm—comparable to previously reported values for high-quality perovskite thin films (Figure 8E).

Funded by the European Union

This project has received funding from the European Union's Horizon Europe research and innovation programme under grant agreement No. 101082176

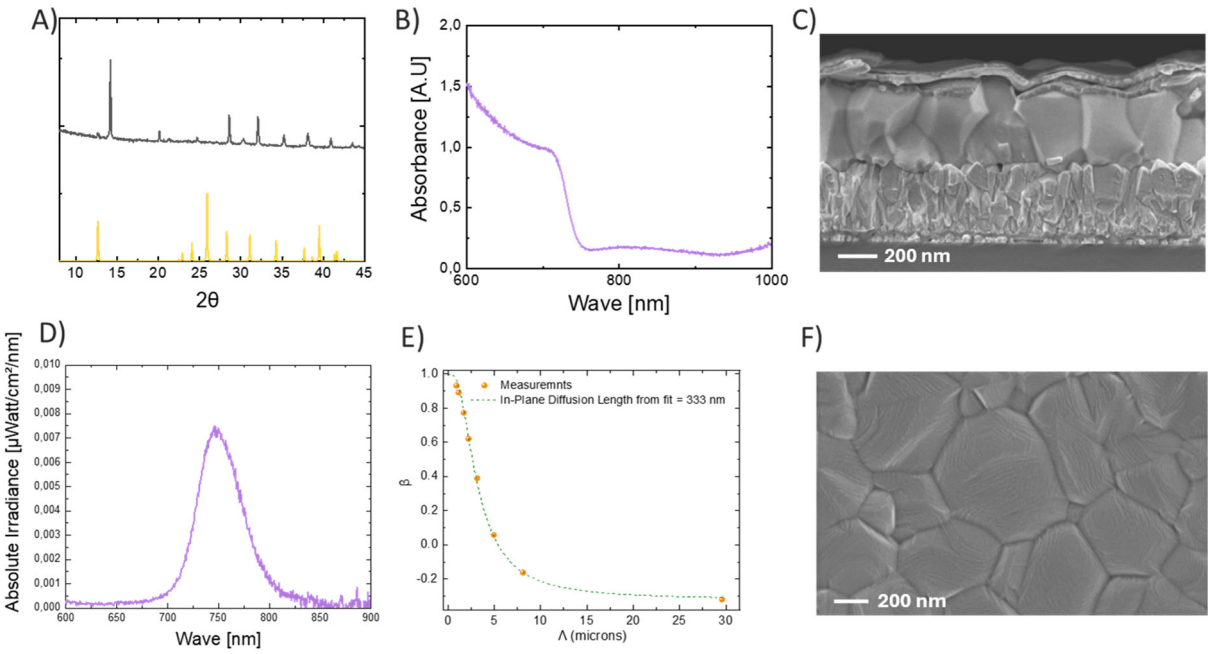

Figure 8: (A) XRD, (B) UV-vis absorbance, (C) SEM cross-section, (D) photoluminescence, (E) diffusion length, and (F) top SEM images of sequentially evaporated $MAPI_3$ films.

1.4.2. Co-evaporated $FAMAPbI_3$

UVEG has developed a reliable and reproducible procedure for the co-evaporation of methylammonium iodide (MAI)-based perovskites using an improved evaporator chamber setup. This setup includes two quartz crystal microbalances (QCMs) dedicated exclusively to monitoring PbI_2 and another organic precursor such as formamidinium iodide (FAI), along with an additional third QCM positioned at the height of the substrates to monitor the total perovskite mass reaching the substrates (perovskite-QCM). Notably, there is no QCM dedicated to MAI; its evaporation is indirectly monitored via the perovskite-QCM. This approach effectively mitigates the fluctuating sublimation rates typically caused by variations in MAI purity, leading to consistently high-performing solar cells that are reproducible over many years.

Thin films of $FA_{1-x}MA_xPbI_3$ perovskite (FAMAPI) were obtained using this evaporator chamber setup. For this experiment, the evaporated films achieved a final thickness of approximately 750 nm. SEM imaging revealed a film composed of very smooth and large crystals uniformly distributed throughout the bulk (Figure 9A). 1H NMR analysis of a dissolved FAMAPI film indicated a stoichiometry of 85% FAI and 15% MAI (Figure 9B), yet XRD analysis also confirmed the presence of unreacted PbI_2 in the perovskite phase (Figure 9C). Moreover, according to the XRD, the FAMAPI film exist in the cubic alpha-phase, with no preferred orientation with respect to the substrate as reflected by intense peaks along [100] and [210] directions. The band gap of the films was measured to be 1.51 eV based on the peak of the photoluminescence (PL) spectrum (Figure 9D), and the films exhibited a photoluminescence quantum yield (PLQY) of 0.23%.

Funded by the European Union

This project has received funding from the European Union's Horizon Europe research and innovation programme under grant agreement No. 101082176

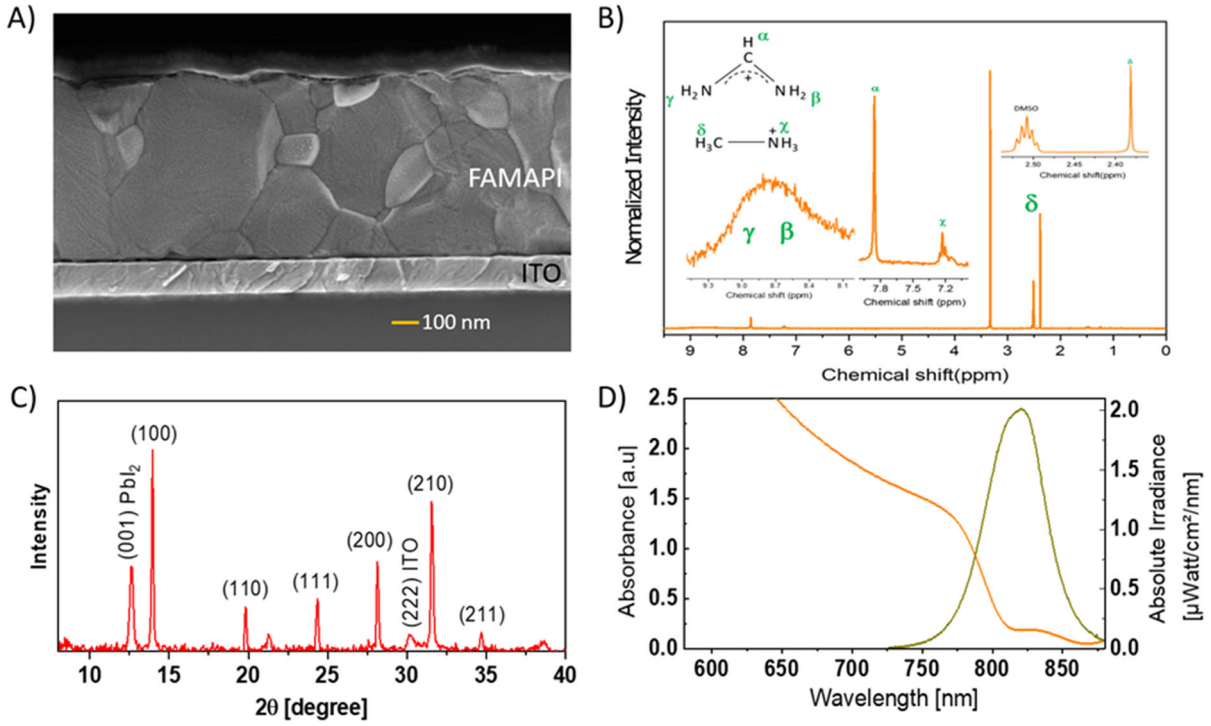

Figure 9 A) SEM image, B) 1H NMR spectra, C) XRD diffractogram, D) absorption and PL spectra of the FAMAPI film deposited on glass/ITO, developed at UVEG.

1.4.3. Co-evaporated $MAFAPbI_3$

Similarly to the section above, thin films of $MA_{1-x}FA_xPbI_3$ perovskite (MAFAPI), with a higher methylammonium content than FAMAPI, were deposited at UVEG using the same evaporator chamber setup. For these films, the deposition parameters were adjusted by decreasing the FAI evaporation rate and increasing the MAI evaporation rate. As shown in Figure 10, the final thickness of the evaporated MAFAPI films was around 520 nm, with very smooth and large crystals uniformly spread across the entire bulk of the film. $_1$H NMR analysis of a dissolved MAFAPI film revealed a stoichiometry of 70% MAI and 30% FAI, and these films also show a slight excess of PbI_2 in the perovskite phase as confirmed by XRD. The XRD diffractogram also confirms the perovskite exist in the cubic alpha-phase, but preferred orientation along the [111] plane. The band gap is 1.57 eV based on the peak of the PL spectrum, and the PLQY of the films is 0.25%.

Funded by the European Union
This project has received funding from the European Union's Horizon Europe research and innovation programme under grant agreement No. 101082176

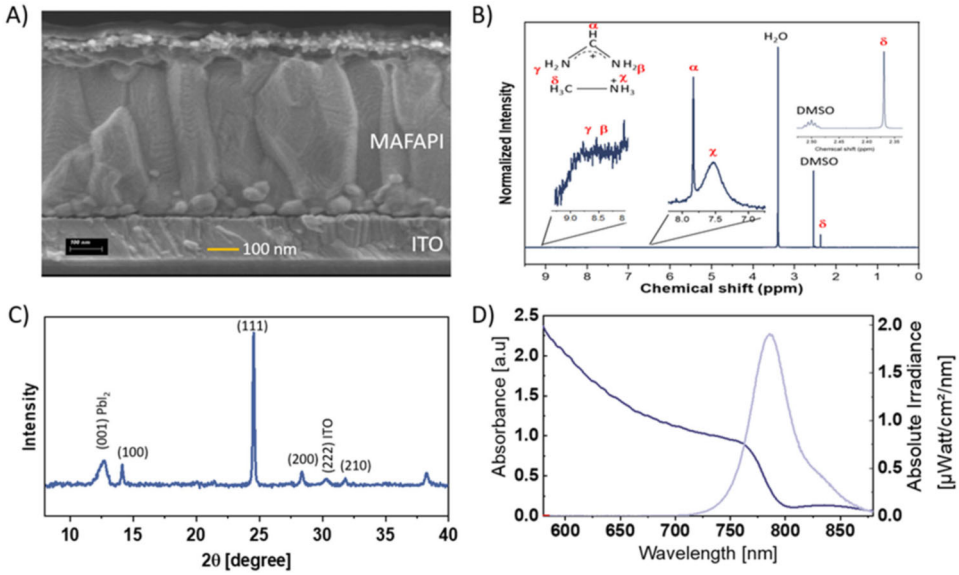

Figure 10: A) SEM image, B) 1H NMR spectra, C) XRD diffractogram, D) absorption and PL spectra of the MAFAPI film deposited on glass/ITO, developed at UVEG.

1.4.4. Co-evaporated $CsFAPbI_3$

A third perovskite was also developed at UVEG, substituting MAI with CsI to form $FA_{1-x}Cs_xPbI_3$ (CsFAPI). The characterization of these films is shown in Figure 11. For this experiment, the evaporated films achieved a final thickness of approximately 500 nm. XRD analysis confirmed the formation of the cubic alpha-phase with intense peaks along the [100] and [200] planes, and with almost no signs of PbI_2. The band gap of the films was measured to be 1.62 eV based on the peak of the photoluminescence (PL) spectrum, with PLQY of 0.60%.

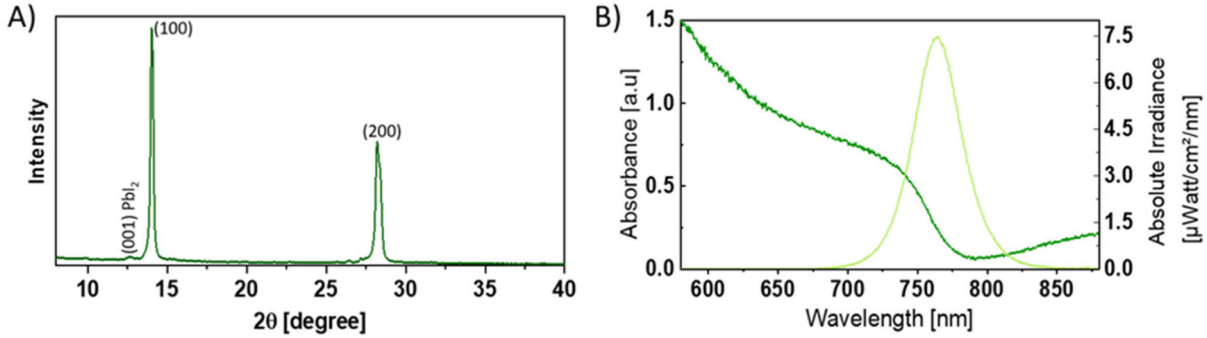

Figure 11: A) XRD diffractogram, B) absorption and PL spectra of the CsFAPI film deposited on glass/ITO, developed at UVEG.

1.4.5. Other sequentially evaporated and co-evaporated perovskites

UOXF developed medium bandgap (1.5 - 1.7 eV) perovskites via two different deposition methods, co-evaporation and sequential evaporation. In both cases the targeted perovskite formulation is $Cs_nFA_{1-n}PbI_3$ with $PbCl_2$ used as crystallization promoter.

Funded by the European Union

This project has received funding from the European Union's Horizon Europe research and innovation programme under grant agreement No. 101082176

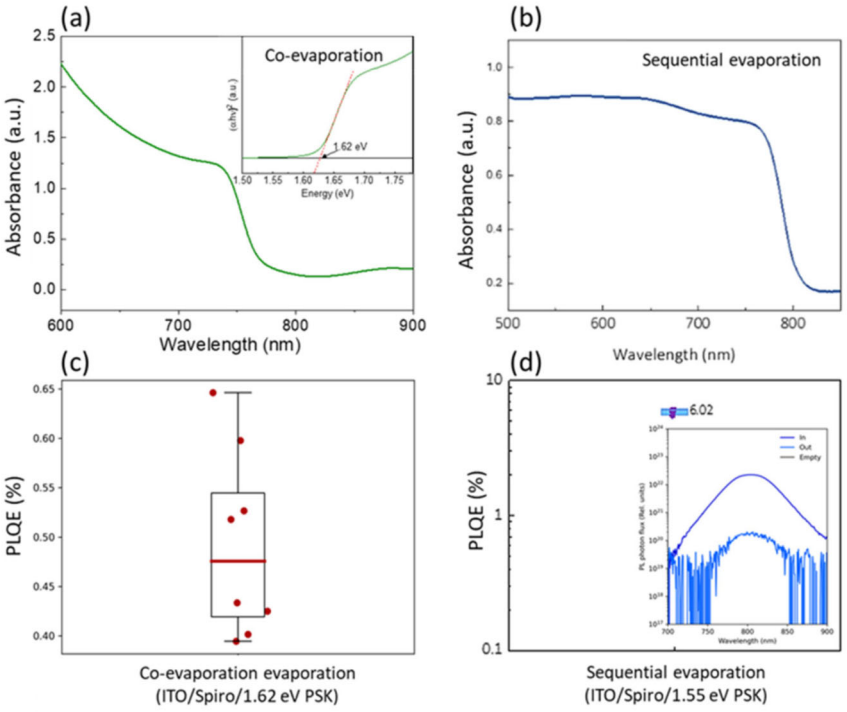

Figure 12: (a) Absorbance spectra of the co-evaporated mid bandgap perovskite films. (b) Absorbance spectra of the sequential-evaporated mid bandgap perovskite films. (c) PLQY of the co-evaporated mid bandgap perovskite films. The samples were prepared on the hole-selective layer resulting in half-stacks with the structure: glass/ITO/Spiro-TTB/perovskite. (d) PLQY of the sequentially evaporated mid-bandgap perovskite films. The samples were also half-stacks with the structure: glass/ITO/Spiro-TTB/perovskite.

The co-evaporated films have an optical bandgap of approximately 1.62 eV, as shown from the absorbance spectrum in Figure 12**a** (inset: Tauc plot to estimate the bandgap). The absorbance spectrum of the sequentially evaporated perovskite films is displayed in Figure 12**b.** The sequentially evaporated films have a smaller optical bandgap of around 1.55 eV. Both types of films exhibit high absorption coefficient as from their absorbance spectra. UOXF measured the PLQY of the perovskite films with the hole-selective layer-based sample stack. The box plot of the PLQY values measured using the co-evaporated film is displayed in Figure 12**c**. The highest PLQY for the co-evaporated perovskite films is about 0.65%, corresponding to a maximum device open-circuit voltage ($V_{oc,PLQY}$) of 1.215 V, which represents a ≈ 9.6 % loss compared to the maximum attainable V_{oc} ($V_{oc,IDEAL}$, in the radiative limit, with 100% PLQY) of 1.345 V. The photoluminescence spectrum and the corresponding box plot of the PLQY values measured on the sequentially evaporated perovskite films are displayed in Figure 12**d**. The sequentially evaporated films exhibit a much higher PLQY of 6.0%, indicating a device V_{oc} of 1.197 V and a ≈ 5.7% loss compared to the ideal V_{oc} value of 1.269 V for a 1.55 eV bandgap (Table 1).

Table 1: Theoretical and experimental V_{oc} loss in the co-evaporated and sequentially evaporated perovskite films.

SAMPLE (half stacks)	*$V_{oc,IDEAL}$ (V)*	*$PLQY_{EXP}$ (%)*	*$V_{oc,PLQY}$ (V)*	*$V_{oc,LOSS}$ (%)*
co-evaporated perovskite, 1.62 eV	1.345	0.65	1.215	9.657
Sequentially evaporated perovskite, 1.55 eV	1.279	6.02	1.196	5.713

Funded by the European Union
This project has received funding from the European Union's Horizon Europe research and innovation programme under grant agreement No. 101082176

1.5. Very wide bandgap perovskite films (>1.7 eV)

1.5.1. Sequentially evaporated CsFAPb($I_{0.5}Br_{0.5}$)$_3$ with 1.95 eV

UOXF developed very wide bandgap perovskite films using a sequential vacuum deposition method. The method consists in co-evaporating the inorganic halides (CsX and PbX_2, X = I, Br) and then coat them with a layer of FAI. Upon annealing, the inorganic scaffold is converted to a hybrid perovskite. To achieve bandgap close to 2 eV, the I:Br ratio should be approximately 1:1, hence mixed CsFA formulation need to be used to avoid spontaneous halide segregation. Figure 13a shows the optical absorption spectrum of a CsFAPb($I_{0.5}Br_{0.5}$)$_3$ perovskite film, showing a sharp absorption onset close to 600 nm. The PL spectrum (Figure 13b) is centred at 610 nm (2.03 eV), confirming the formation of a perovskite with optical bandgap of approximately 2 eV. The XRD pattern shows that the films are highly crystalline (high signal-to-noise ratio) with no peaks corresponding to residual unconverted phases.

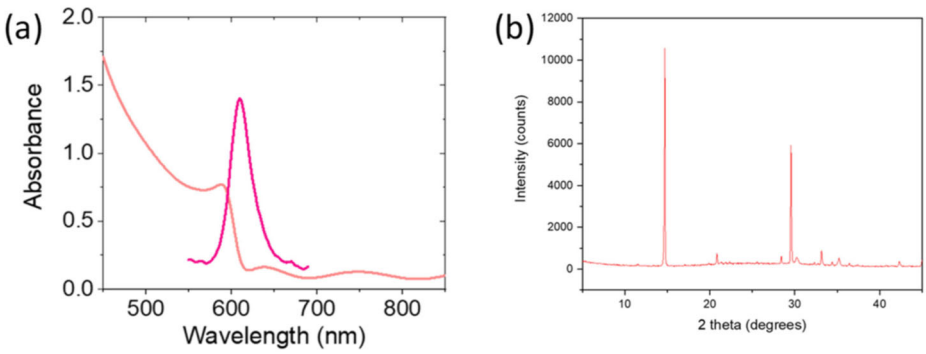

Figure 13: (a) Absorption and photoluminescence spectra of a 1.95 eV CsFA-based perovskite film. (b) X-ray diffraction pattern of the same material.

1.5.2. Co-evaporated fully inorganic Cs-based perovskites with bandgap in the 1.9-2.0 eV range

Fully co-evaporated perovskite films with bandgaps >1.7 eV have been prototyped at UVEG, specifically targeting the 1.9 – 2.0 eV range, which is useful for coloured solar cells and indoor photovoltaics. This bandgap range is particularly challenging because it requires an almost equal concentration of iodide and bromide, which unavoidably results in photoinduced halide segregation and phase instability. For this reason, UVEG developed fully inorganic perovskites of the type $CsPbIBr_2$, that are less prone to halide segregation thanks to the lower structural tolerance factor. The initial composition was obtained using a combinatorial approach previously developed at UVEG for the co-evaporation of complex perovskite mixtures.

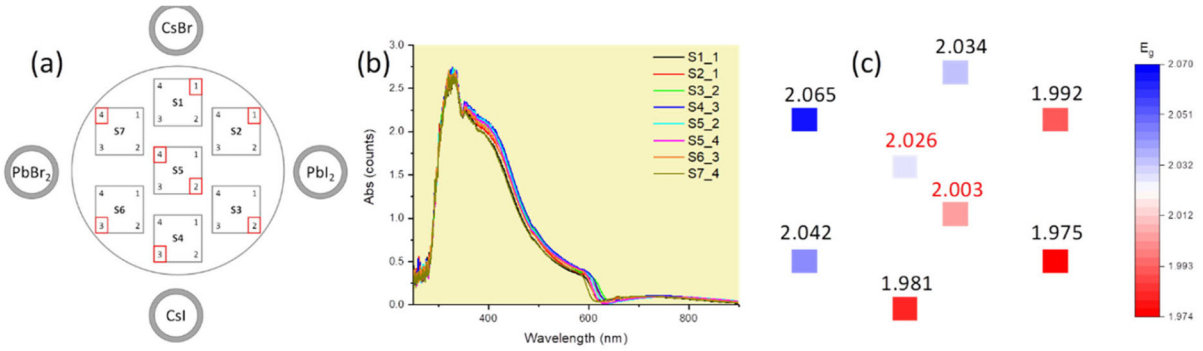

Figure 14: (a) Configuration for a perovskite deposition without rotation using CsI, CsBr, PbI_2 and $PbBr_2$ as

Funded by the European Union
This project has received funding from the European Union's Horizon Europe research and innovation programme under grant agreement No. 101082176

precursors and 7 substrates (S1 – S7). The red squares indicate the area where the (b) optical absorption spectra are measured. From the optical data, a (c) simple map of the energy bandgap of the perovskite over the different substrates is obtained.

It consists in the co-evaporation of the different perovskite precursors using a fixed sample holder: hence compositional gradients are obtained which can be analysed to identify the material of interest. An example of the perovskite bandgaps obtained with an evaporation without rotation after a few iterations to optimize the deposition rates is included in Figure 14**.** Perovskites with bandgap very close to 2.0 eV can be readily obtained using the following deposition rates: CsI 0.6 Å/s, CsBr 0.5 Å/s, PbI2 0.5 Å/s, PbBr2 0.6 Å/s. The films were tested for photostability by measuring their photoluminescence (PL) under continuous laser illumination at 1 sun equivalent carrier concentration. As depicted in Figure 15, the pristine CsPbIBr2 films exhibit a red shifted PL component after 30 minutes' irradiation, suggesting halide segregation. Hence other compounds were co-evaporated with the aim of stabilizing the perovskite formulation. From this screening, the co-evaporation of benzylammonium iodide or rubidium iodide were found to stabilize the PL spectra under irradiation, albeit with a small loss in PL intensity, which is more prominent in the case of doping with RbI. These stable and promising materials were transferred to WP2 for device integration and characterization.

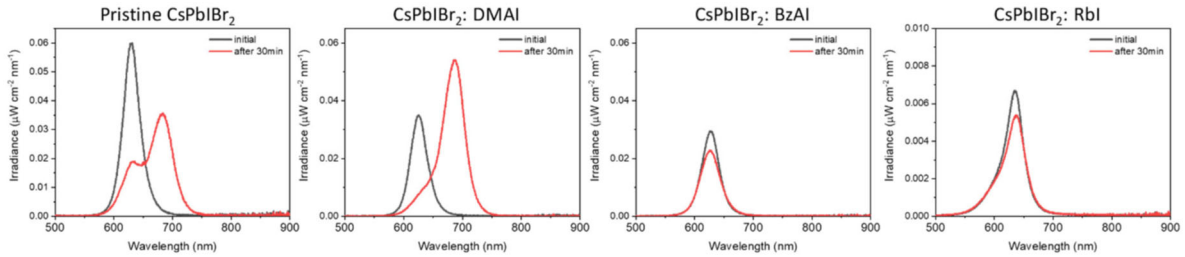

Figure 15: Initial (black) PL spectra and (red) after 30 minutes of continuous irradiation with a 520 nm laser for pristine $CsPbIBr_2$ films (left) and films substituted with different compounds (DMA: dimethylammonium; BzAI: benzylammonium iodide; RbI: rubidium iodide).

1.6. Theoretical analysis with DFT models

CNR investigated the defects chemistry of metal halide perovskites (MHP) to identify the nature of the defects limiting the efficiency and stability of the perovskites with different compositions and the potential strategies to minimize their detrimental impact on the optoelectronic properties.

1.6.1. Defect chemistry as a function of perovskite composition

The defects chemistry of metal halide perovskites (MHP) with low (1.3 eV), medium (1.5-1.6 eV) and high (1.9 eV) band gaps has been analyzed based on density functional theory (DFT) calculations. Defect analysis has been focused on the $FASnI_3$, $FAPb_{0.5}Sn_{0.5}I_3$, $FAPbI_3$ and $FAPbBr_{1.5}I_{1.5}$ as the prototypes for the low, medium and high band gap materials. In Figure 23 the defect formation energies (DFE) of native defects calculated in I-medium conditions are reported for the investigated compositions.

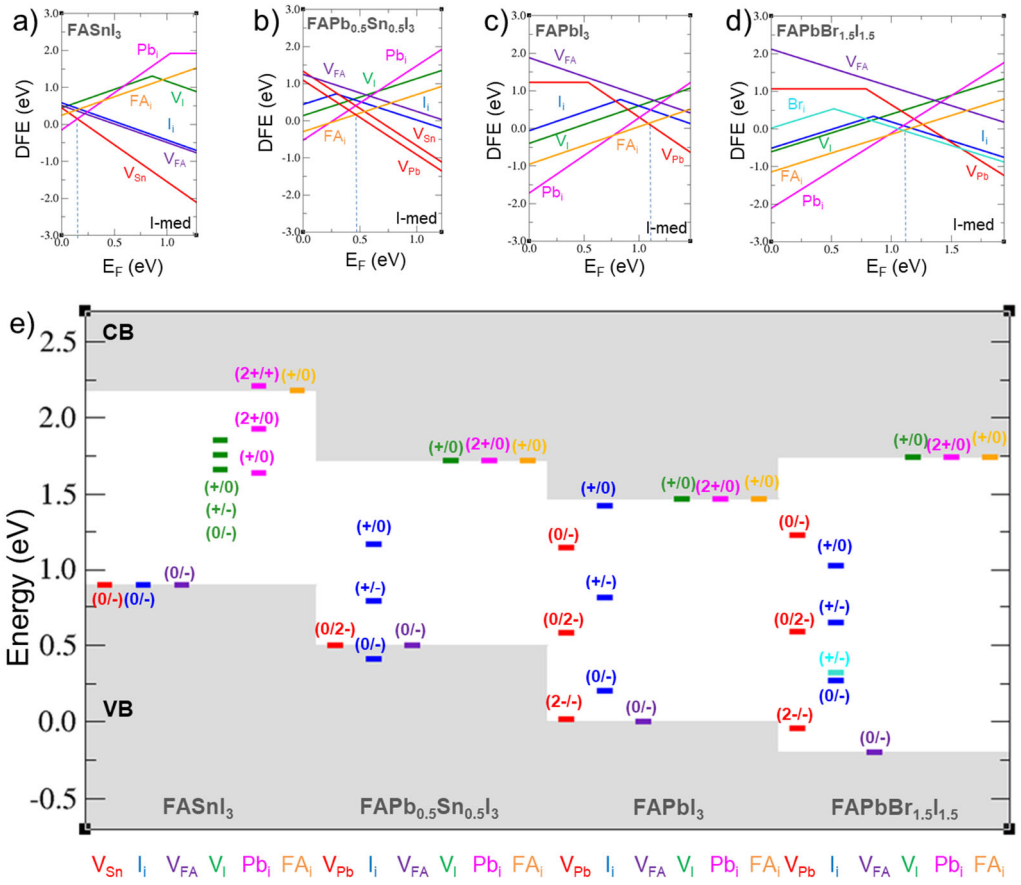

Figure 16 a-d) Calculated DFEs of native defects in the FASnI3, FAPb0.5Sn0.5I3, FAPbI3 and FAPbBr1.5I1.5 perovskites in I-medium conditions of growth (PBE0-SOC level of theory); e) associated thermodynamic ionization levels, the VBM of the FAPbI3 has been set to zero.

In $FAPbI_3$ the most stable defects are formamidinium interstitials (FA_i) and lead vacancies (V_{Pb}) which pin the Fermi level at around 1.1 eV above the VBM. In the high band gap $FAPbBr_{1.5}I_{1.5}$ perovskite the native Fermi level is pinned at a similar value by FA_i and bromide interstitials (Br_i). This indicates that the $FAPbI_3$ and $FAPbBr_{1.5}I_{1.5}$ are essentially intrinsic, i.e. the density of defects is higher with respect to that of charge carriers.

The analysis of the thermodynamic ionization levels (TIL) in Figure 16 highlights that the only defects introducing ionization levels deep in the band gap of the $FAPbI_3$ and $FAPbBr_{1.5}I_{1.5}$ are V_{Pb} and I_i. These defects are stable in the negative forms at the native Fermi level and can trap photo-generated holes through the (2-/-) and (0/-) transitions placed at 0.14 (0.02) eV and 0.47 (0.20) eV above the VBM of the $FAPbBr_{1.5}I_{1.5}$ ($FAPbI_3$). Upon hole trapping on the I_i^- and V_{Pb}^{2-} defects two iodides are bound at about 3.2 Å to form a radical I_2^- dimer, see Figure 17. The trapping of a second hole leads to the formation of a I_3^- trimer, where the iodine is in the +I oxidation state and it is bound to two lattice iodides at a distance of 2.9 Å (see Figure 17). In the case of the V_{Pb}^0 defect two holes are trapped to form the trimer and one iodide vacancy. The Fermi level transitions associated to the oxidation of iodide from -I to +I states are the (+/-) and the (0/2-) transitions for I_i and V_{Pb}, placed at 0.81 (0.85) eV and 0.58 (0.79) eV, respectively in $FAPbI_3$ ($FAPbBr_{1.5}I_{1.5}$).

Funded by the European Union
This project has received funding from the European Union's Horizon Europe research and innovation programme under grant agreement No. 101082176

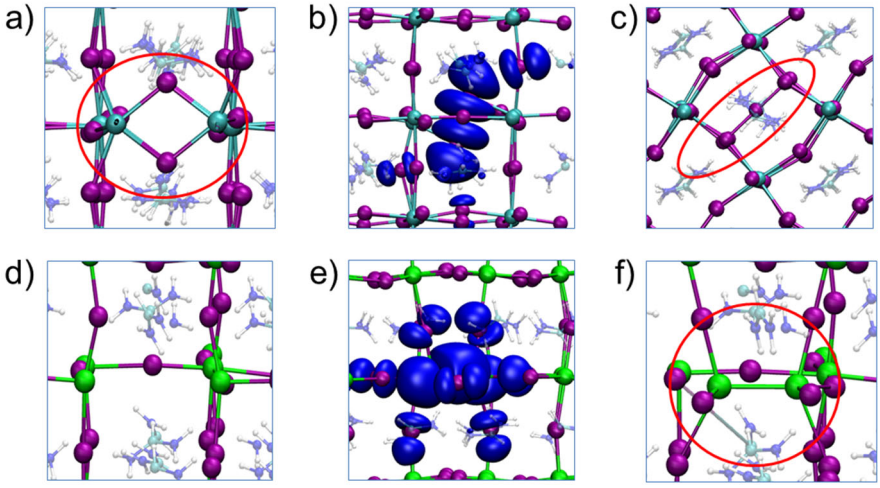

Figure 17 Equilibrium structures of a) I_i^-; b) I_i^0 with the density plot of the trapped hole; c) I_i^+ in the $FAPbI_3$ perovskite and d) V_I^+; e) V_I^0 with the density plot of the trapped electron; f) V_I^- in the $FASnI_3$ perovskite.

Moving to the low band gap perovskites, a progressive increase in energy of the VBM is observed, i.e. 0.5 and 0.9 eV for the $FAPb_{0.5}Sn_{0.5}I_3$ and the $FASnI_3$ perovskites, respectively, with respect to $FAPbI_3$. The most stable defects in $FAPb_{0.5}Sn_{0.5}I_3$ are FA_i and V_{Pb}, which pin the Fermi level to ~0.50 eV above the VBM. In $FAPb_{0.5}Sn_{0.5}I_3$ I_i shows deep (+/-) and (+/0) transitions placed at 0.28 and 0.67 eV above the VBM, but such transitions do not impact the optoelectronic properties due to the low cross section of the two-hole capture process and the instability of the I_i^+ defect at the intrinsic Fermi level of the perovskite. The up-shift in energy of the VBM also deactivates the deep transitions associated with the V_{Pb} defect, that is only stable in the 2- charged state across the Fermi level.

By increasing the tin content up to the full $FASnI_3$ perovskite a large stabilization (destabilization) of the V_{Sn} (Sn_i) defect is observed. This induces a shift of the Fermi level close to the VBM (0.15 eV), indicating a heavy p-doped material ($[h+] = 10^{18}$ cm^{-3}). Due to the parallel increase of the CBM, deep electron traps associated with iodide vacancies and tin interstitials arise in the band gap of the material. Both V_I^+ and Sn_i^{2+} defects can trap electron by leading to the formation of tin dimers, see Figure 17.

Overall, moving from medium-high band gap to low band gap perovskites a suppression of iodine-related hole traps and the deepening of tin-related electron traps is observed. This is accompanied by an increase of p-doping of the material.

The impact of the organic cation on the defects chemistry of the perovskites has been also analyzed through the comparison of the defects energetics in $FAPbI_3$ and $MAPbI_3$, see Figure 18.

Funded by the European Union

This project has received funding from the European Union's Horizon Europe research and innovation programme under grant agreement No. 101082176

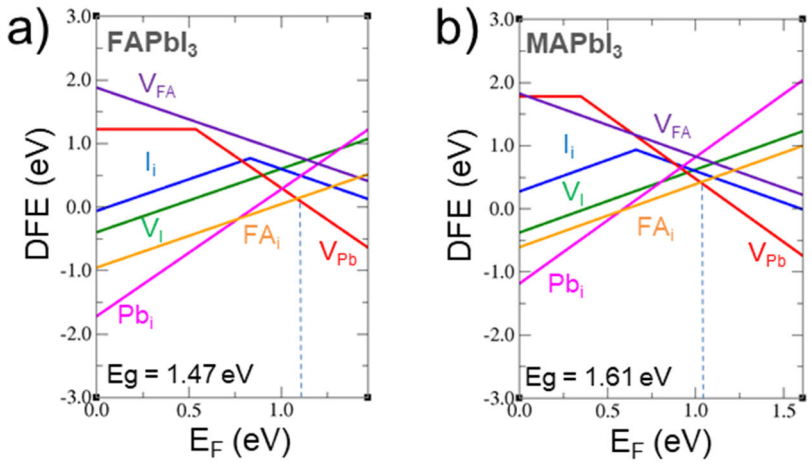

Figure 18 DFEs of native defects (I-medium conditions, PBE0-SOC) in a) FAPbI3 and b) MAPbI3.

As can be seen, the DFEs of native defects in $FAPbI_3$ and $MAPbI_3$ are rather similar, except for some defects showing lower DFEs in the $FAPbI_3$ perovskite, particularly I_i^+, FA_i^+ and Pb_i^{2+} donors.

The effects of the cation alloying has been analyzed by the direct comparison of the DFEs (PBE level) of a selected list of defects in the FA, FACs, FAMA and MA compositions, see Table 2. The cation alloying of $FAPbI_3$ with 25% of Cs increases the thermodynamic stability of the lattice towards the decomposition to precursors and slightly increases the energy of formation of V_{PbI2} to values comparable to $MAPbI_3$, while in the case of MA alloying no sensible variations are reported. These results indicate that the cation alloying of FA perovskites with Cs and MA only slightly impacts the defect chemistry of the material.

Table 2 Cation effects on the DFEs of native defects in lead perovskites. Heat of formation of the phases vs precursors $\Delta_f H$ and DFE values calculated at the VBM. DFEs are calculated in I-medium conditions at the PBE level.

	$FAPbI_3$	**$FA_{0.75}Cs_{0.25}PbI_3$**	**$FA_{0.75}MA_{0.25}PbI_3$**	**$MAPbI_3$**
$\Delta_f H$ (meV)	+80	+31	+86	+6
DFE@VBM (eV)				
V_I^+	-0.11	-0.23	-0.19	0.01
I_i^-	1.25	1.08	1.10	1.22
I_i^+	0.24	0.17	0.19	0.62
V_{Pb}^{2-}	1.50	1.60	-	1.75
V_{Pb}^0	1.00	-	-	1.53
Pb_i^{2+}	-0.91	-0.81	-	-0.18
FA_i^+	-0.45	-0.33	-	(MA_i^+) 0.30
V_{FA}^-	1.36	1.40	-	(V_{MA}^-) 1.47
V_{PbI2}	0.49	0.65	0.50	0.62
V_{FAI}	0.99	0.92	1.02	(V_{MAI}) 1.08

Funded by the European Union
This project has received funding from the European Union's Horizon Europe research and innovation programme under grant agreement No. 101082176

1.6.2. Impact of defects and potential strategies to improve stability and efficiency

Medium-high band gap MHP

Non-radiative recombination and efficiency. According to the defect analysis, I_i and lead vacancies V_{Pb} introduce deep recombination levels in the band gap of $FAPbI_3$ and $FAPbBr_{1.5}I_{1.5}$ by increasing non-radiative recombination and lowering the efficiency of the associated solar cell devices. This analysis highlights that *I-rich conditions should be avoided in the crystallization of the perovskites and precursors should be purified from I_2 in order to prevent the incorporation of excess iodide in the lattice.* This condition is simulated in the DFE diagram of Figure 19, where the DFEs of native defects in $FAPbI_3$ in I-rich conditions are reported. As can be seen, I_i^+ and V_{Pb}^{2-} , both are traps, are highly stable and in this conditions they occur in high densities, decreasing the efficiency of the device.

Photo-stability. Experiments demonstrate that I_2 expulsion at the grain boundaries is a photo-activated process in lead-based perovskites. In halide-mixed perovskites, I_2 emission occurs in parallel to the photo-demixing of the material to give I-rich and Br-rich compositions, highlighting that the two processes are correlated.[]

The emission of I_2 in lead and halide-mixed perovskites may be explained by the deep trapping activity of iodide defects. With high densities of photo-generated holes, such as under intense irradiation, the sequential trapping of two holes on the I_i^- and V_{Pb}^{2-} sites induces the formation of the oxidized form of interstitial, i.e. I_i^+. The process starts at the defect sites, by proceeding to lattice iodides following the reactions

$I_i^- + 2h^+ = I_i^+$ (-1.02 / -0.60 eV, FA / MA PbI_3)

$I_I^0 + 2h^+ = V_I^+ + I_i^+$ (+0.05 / 0.56 eV, FA / MA PbI_3)

DFT simulations reveals that, while the I_i^+ / I_i^- couple is thermodynamically stable in the bulk of the perovskite, it is less stable than the adsorbed I_2 molecule at the surface, e.g. by 0.73 eV in $MAPbBr_{1.5}I_{1.5}$ (see Figure 39b), highlighting that the emission of I_2 can spontaneously evolve from these defects. Previous work, however, highlighted a fairly high barrier to the direct reaction of the couple (0.3 eV), indicating that I_2 emission is activated by light through the trapping of electron and holes on the defect couple and the formation of I_2^- radicals, which readily react to form I_2, i.e. $I_i^+ + I_i^- + 1e^- + 1h^+ = 2\ I_i^0 = I_2$.[The expulsion of I_2 can be also activated by the direct photolysis of I_i^+, i.e. $I_3^- + hv = I_2 + I^-$.

Funded by the European Union
This project has received funding from the European Union's Horizon Europe research and innovation programme under grant agreement No. 101082176

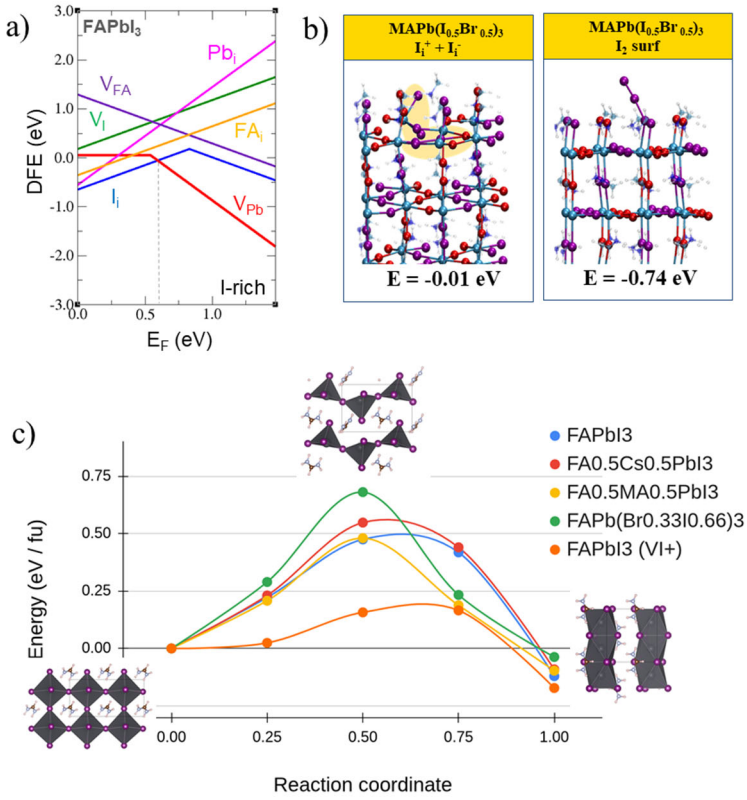

Figure 19 a) DFEs of native defects in FAPbI3 in I-rich conditions (PBE0-SOC); b) Structures and relative stability of the Ii+ / Ii- couple and the I2 molecules at the surface of MAPbBr1.5I1.5 surface.

In FA compositions the disruption of the iodide sub-lattice induced by photo-degradation activates the transition from the active α- to the inactive δ-phase. In Figure 39c the barrier of the phase transition, as calculated from a linear transit approach, is reported for different composition of the FA perovskites and in presence of an iodide vacancy, simulating highly disordered lattice. As can be observed, a decrease of the transition barrier from 0.47 to 0.17 eV is reported.

A parameter to evaluate the photo-stability of the perovskites is the energy of formation of the I_i^+ / I_i^- couple in the lattice. Specifically, perovskites showing an increased stability of the couple are more sensible to photo-degradation under light through the emission of I_2. The energy of formation of the I_i^+ / I_i^- couple has been monitored for several ABX_3 compositions with different organic cations (A = FA, MA, Cs), metals (B = Pb, Sn) and halides (X = I, Br), see Table 3. In parallel to the energy of formation of the interstitial couple, the position of the (+/-) transition in the band gap, indicating the relative stability of I_i^+ vs I_i^- is reported.

Table 3 Heat of formation of the perovskites vs precursors (ΔfH, mixing entropy included), energy position of the (+/-) transition in the band gap vs VBM and calculated DFEs of the (Ii+ / Ii-) couple (calculated as the sum of the DFEs of the non-interacting Ii+ in I-rich conditions). All values are calculated at the PBE level.

system	$\Delta_f H$ (eV)	TIL (+/-) (eV)	DFE (I_i^+ / I_i^-) (eV)

Funded by the European Union
This project has received funding from the European Union's Horizon Europe research and innovation programme under grant agreement No. 101082176

$FAPbBr_{1.5}I_{1.5}$	-0.02	0.46	1.01
$FAPbI_3$	0.08	0.51	0.40
$FA_{0.75}Cs_{0.25}PbI_3$	0.02	0.46	0.16
$FA_{0.75}MA_{0.25}PbI_3$	0.08	0.45	0.20
$FAPb_{0.5}Sn_{0.5}I_3$	0.01	0.09	0.58
$MAPbBr_{1.5}I_{1.5}$	-0.04	0.34	1.01
$MAPbI_3$	0.01	0.30	0.86
$MAPb_{0.5}Sn_{0.5}I_3$	-0.04	-	-
$CsPbBr_3$	-0.31	0.02	1.40
$CsPbBr_{1.5}I_{1.5}$	-0.21	0.18	0.96
$CsPbI_3$	-0.14	0.24	0.92

The analysis of the energy of formation of the I_i^+ / I_i^- couple in the different compositions highlights that it is more easily formed in less stable compositions, by following the thermodynamic stability of the lattice. The stability of the couple is decreased by moving from FA to MA to Cs and by moving from full I to the full Br composition. Similarly, a shallowing of the (+/-) transition, indicative of a reduced stability of the I_i^+ form of the interstitial with respect to I_i^-, is observed by moving from FA to MA to Cs and from the full-iodide to the mixed-bromide phases. The strongest destabilization of the I_i^+ is reported for the tin alloying, in agreement with the increased energy of the VBM, as discussed in the defect analysis section. Specifically, the alloying with the 50% of tin leads to a drastic shallowing of the (+/-) transition in $FAPb_{0.5}Sn_{0.5}I_3$ (0.09 eV) and in $MAPb_{0.5}Sn_{0.5}I_3$ such transition is nearly zero and the I_i^- is the only stable defect. The analysis of the α- δ-phase transition barrier for the different compositions, on the other hand, highlights that a sensible increase of the barrier is obtained only by Br-alloying, indicating that the alloying of FA with Cs, MA or Sn mainly stabilized the phase through a thermodynamic stabilization of the lattice.

Funded by the European Union

This project has received funding from the European Union's Horizon Europe research and innovation programme under grant agreement No. 101082176

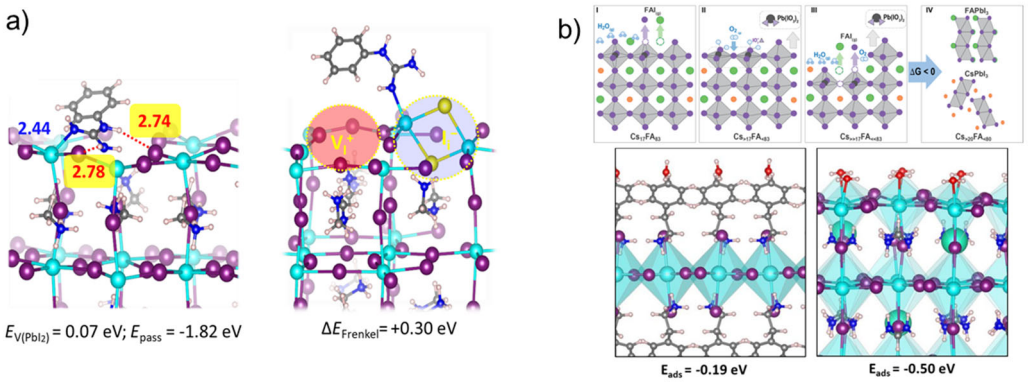

Figure 20 a) Passivation by the pGUA molecule; b) schematics of the degradation under O2/H2O and hydrophobic effects of the PEA cation

These results show that, in order to improve the photo-stability of medium-high band gap MHPs, it is critical to passivate lead ions and reduce ionic disorder, particularly at the surface, where I_2 can nucleate. Potential passivating agents are molecule binders, such as amines, phosphonic and carboxilic acids, or polymers, e.g. polyethilenoxide (PEO). We showed that the use of 1-phenylguanidine (PGua), as an additive in solution processed perovskites, beside retarding the perovskite crystallization process and forming more homogeneous and less defective films, is able to efficiently coordinated lead ions at the surface and suppress Frenkel defects, see Figure 20a. This reflects in more efficient and operational stable devices. Similar effects have been reported for the sulfonium-based DMPESI molecule. It can passivate surface defects, enhance the thermodynamic stability of black $FAPbI_3$, preventing phase transition to the δ phase. The treatment with phenylethylammonium iodide (PEAI) can protect the perovskite by forming a compact and hydrophobic capping layer on top of the surface, by hindering the incorporation of water and the ambient-induced formation of defects, as illustrated in Figure 40b.

An alternative strategy which can be tested to enhance the photo-stability of high band gap perovskites is the alloying with Sn and Br, even though this introduces additional problems connected to the stability of tin against external agents (O_2, H_2O) which can be mitigated by efficient encapsulation techniques. DFT simulations showed that, differently from $MAPbBr_{1.5}I_{1.5}$, at the $MASnBr_{1.5}I_{1.5}$ surface the recombination of $2I_i^-$ + 2h+ ($2I_i^0$) to form I_2 is thermodynamically unfavorable, highlighting that I_2 emission is hindered and it cannot trigger the photo-demixing of the perovskite. This has been confirmed by experiments, showing that halide-mixed tin perovskites are more tolerant against the photo-demixing compared to lead perovskites.

Low band gap

p-doping and efficiency. As discussed in the defect chemistry section, the intermediate $FAPb_{0.5}Sn_{0.5}I_3$ composition does not show deep levels in the band gap, except for the (+/-) and (+/0) transitions of I_i, which however do not increase non-radiative recombination. The analysis of the lattice stability highlights that the metal-mixed composition is stable against the phase de-mixing in dark
$FA(MA)Pb_{0.5}Sn_{0.5}I_3$ = ½ $FA(MA)PbI_3$ + ½ $FA(MA)SnI_3$, (FA +0.02 eV, MA +0.01 eV)

Funded by the European Union
This project has received funding from the European Union's Horizon Europe research and innovation programme under grant agreement No. 101082176

Although thermodynamically stable and potentially trap-free, lead-tin perovskites with comparable amounts of tin and lead partially inherit the photo-instability problem of full lead perovskites due to the partial stability of the I_i^+ in the bulk FA composition.
By increasing the tin content up to the $FASnI_3$ perovskite leads to the complete quenching of the deep levels associated to I_i. The most critical factor largely reducing the efficiency of tin-rich compositions is the remarkable stabilization of acceptor defects, particularly V_{Sn}, causing a strong increase of the p-doping with predicted hole densities in the range 10^{18}-10^{19} cm^{-3} in $FA/MASnI_3$. The heavy p-doping associated to this composition strongly reduces the efficiency of the associated solar cells compared to the lead-based perovskites.
The use of tin-rich conditions upon crystallization of tin-lead and tin perovskite should be preferred in order to reduce the density of tin vacancies, responsible for the self p-doping. I*t is fundamental to purify precursors from I_2 and Sn(IV) impurities (e.g. SnI_4),* since their inclusion in the lattice aggravates the p-doping of the perovskite through the incorporation of iodine interstitials and the release of the holes to the VBM
$SnI_4 = Sn_{Sn}^0 + 2\ I_I^0 + 2I_i^- + 2h^+$

3. Charge Extraction layers

This part of the deliverable serves as an overview of the research conducted within the VALHALLA consortium, offering insights into the development of electron and hole transporting materials.
KTU developed organic molecules for self-assembled monolayers (SAMs) and thin organic films for hole and electron extraction, UVEG focused on the inorganic electron-selective SnO_2 and the aluminium zinc oxide (AZO) transparent conductor grown by pulsed laser deposition (PLD).

1.7. Materials forming hole selective monolayers

Among the plethora of materials capable of extracting holes from the perovskite layer, KTU focused on molecules capable of forming self-assembled monolayers.

1.7.1. Halogenated carbazole-based materials

KTU has developed a series of halogenated carbazole-based SAM molecules containing phosphonic acid functional group. Carbazole was chosen as a reliable chromophore with a previous track record of good performance in SAM materials, and convenient and straightforward synthesis procedures, which allow for relatively easy functionalization. Different halogens, their position and number of substituents were investigated. The main goal was to compare all these variables and find optimal structure for the most effective carbazole-based halogenated SAM derivative.
Most of the halogenated carbazoles, except for 3,6-difluoro-9*H*-carbazole, are commercially available, thus shortening and streamlining the synthesis procedure. Synthesis of 3,6-halogenated SAMs was performed in a 3-step procedure (Figure 21).

Funded by the European Union
This project has received funding from the European Union's Horizon Europe research and innovation programme under grant agreement No. 101082176

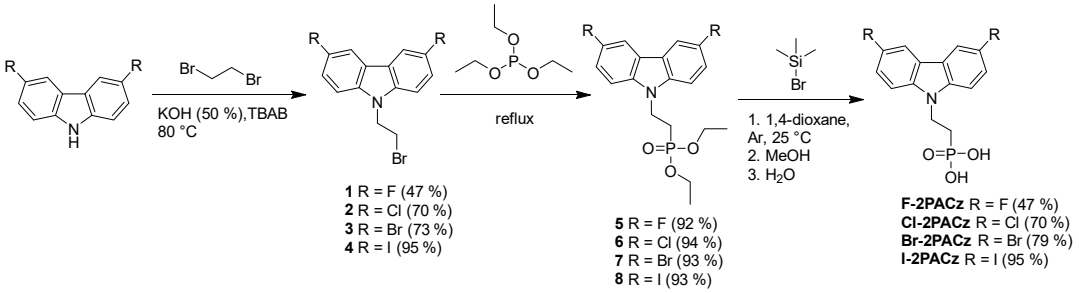

Figure 21 Synthesis of 3,6-halogenated carbazole derivatives containing the phosphonic acid group

Halogenated carbazoles were alkylated by using 50% aqueous solution of KOH and TBAB and 1,2-dibromoethane, which acted both as an alkylation agent and a solvent. Alkylated derivatives further reacted with triethyl phosphite, thus forming intermediate phosphonic acid ethyl esters. The final products, containing the phosphonic acid functional group, were obtained by the hydrolysis of phosphonates, while using bromotrimethylsilane, methanol and water.

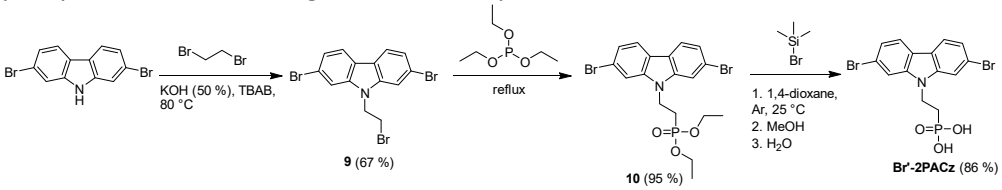

Figure 22 Synthesis of 2,7-dibromocarbazole derivatives containing the phosphonic acid group

To evaluate the influence of the halogen substituent position, 2,7-dibromo-9*H*-carbazole was chosen for the synthesis. **Br'-2PACz** was synthesized *via* a similar synthesis procedure as 3,6-halogenated carbazole analogues (Figure 22).

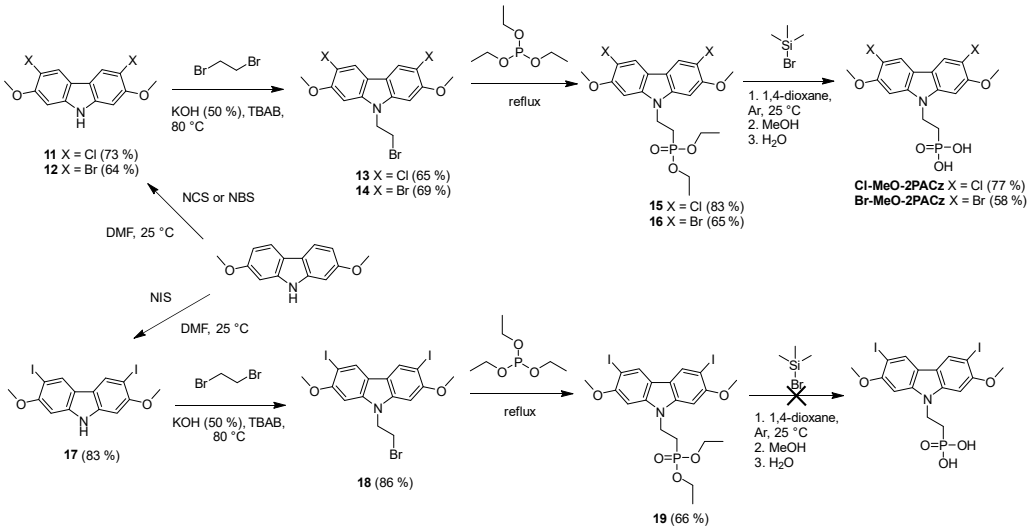

Figure 23 Synthesis of halogen and methoxy substituted carbazole derivatives containing the phosphonic acid group

Finally, methoxy groups were introduced to induce an influence dipole moment due to the presence of both the acceptor and donor functional groups. 2,7-Dimethoxy-9*H*-carbazole was halogenated by using the appropriate halogenation agent, and final materials **Cl-MeO-2PACz** and **Br-MeO-2PACz**, containing chlorine or bromine substituents, respectively, were synthesized *via* a similar 3-step procedure (Figure 23). Iodine containing intermediates **17**, **18** and **19** were synthesized by conducting similar halogenation, alkylation and phosphonylation reactions. However, the hydrolysis reaction of

Funded by the European Union
This project has received funding from the European Union's Horizon Europe research and innovation programme under grant agreement No. 101082176

intermediate **19** was unsuccessful, suggesting side reactions between iodine and methoxy groups in the presence of hydrolysis agent bromotrimethylsilane.

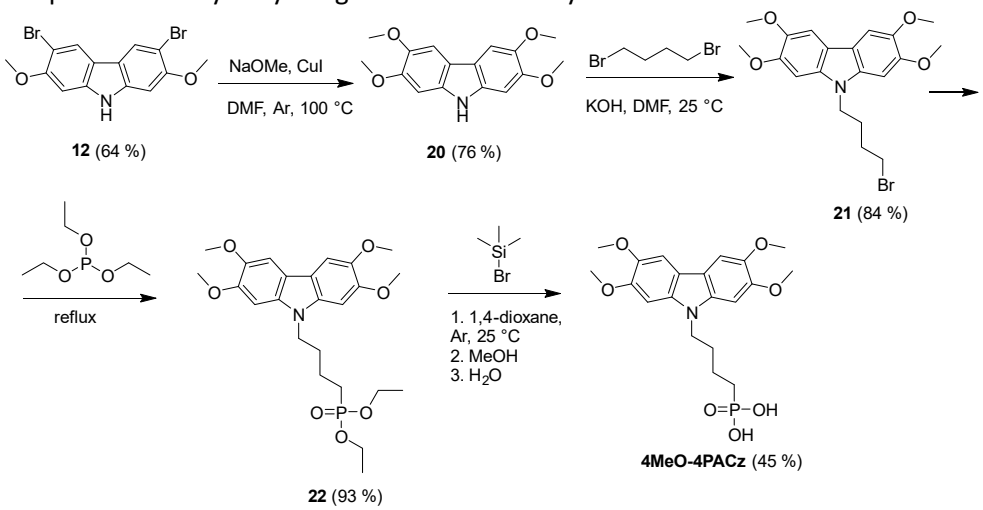

Figure 24 Synthesis of carbazole containing four methoxy groups and phosphonic acid

For comparison with previously synthesized materials and commercial MeO-2PACz, tetra-methoxy substituted carbazole phosphonic acid was obtained *via* intermediate carbazole **12** by using reaction with sodium methoxide in DMF, in the presence of copper (I) iodide, resulting in 2,3,6,7-tetramethoxycarbazole **20** (Figure 24). A similar 3-step alkylation/Arbuzov reaction/hydrolysis procedure was used to produce the final product **4MeO-4PACz**.

The ionization potential (I_p) of the synthesized halogenated SAM materials was measured by using *photoelectron spectroscopy in air* (PESA) measurement Additionally, the work functions of modified ITO substrates were measured by using *Kelvin Probe AFM* so that to evaluate how SAMs influence the ITO surface energy.

Table 4 Measured ionization potential and work function values of the synthesized halogenated SAM derivatives

HTM	I_p [eV]	Work Function [eV]
ITO	–	4.70
Br-2PACz	6.01	5.82
F-2PACz	5.92	5.68
Cl-2PACz	6.05	5.77
I-2PACz	5.92	5.73
Br'-2PACz	5.78	4.78
Cl-MeO-2PACz	5.81	5.60
Br-MeO-2PACz	5.85	5.70
4MeO-4PACz	5.47	–

The results obtained (Table 4) reveal that the introduction of halogen substituents resulted in deeper highest occupied molecular orbital (HOMO) energy levels, compared to 2PACz (5.6 eV) and MeO-2PACz (5.30 eV), which was expected, due to the electron accepting properties of the halogen substituents. Among them, chlorine containing derivative **Cl-2PACz** demonstrated the highest energy level value of -6.05 eV. In contrast 2,7-dimebromo substituted carbazole **Br'-2PACz** stood out from the researched substances by its lowest WF (4.78 eV), thus indicating the influence of the halogen substituents'

Funded by the European Union
This project has received funding from the European Union's Horizon Europe research and innovation programme under grant agreement No. 101082176

position in the carbazole core.
From the results of the primary investigation a series of halogenated carbazoles (F-2PACz, Cl-2PACz, Br-2PACz, I-2PACz, Br'-2PACz) and halogen and methoxy substituted derivatives (Cl-MeO-2PACz, Br-MeO-2PACz) as well as 4MeO-4PACz containing four methoxy groups were selected for further testing in the devices at project partners facilities (WP2, Task 2.1) to determine suitability of this type of materials.

1.7.2. SAM materials containing phosphonic acid functional group and central core interacting with perovskite at the interface

Carbazole-based SAM derivatives, such as 2PACz, MeO-2PACz or Me-4PACz, are well-known materials, currently being investigated in a wide range of optoelectronics. More and more materials are being developed as follow ups to widen the SAM research field. This includes both carbazole and non-carbazole molecules containing the phosphonic acid functional group.
KTU has focused on development of a series of non-carbazole SAMs. The chromophores that were chosen for synthesis were picked to be structurally close to well performing 2PACz, and their central cores would bear significant but not drastic chemical structure differences, thus allowing us to investigate the performance of the SAMs with small changes in the structure and, hopefully, better understand the structure-performance relation.
Another strategy to broaden the range of the currently used SAM materials beyond 2PACz or Me-4PACz is to increase their functionality by incorporating additional functional groups. These groups can be used to tune the energy levels, change the surface wetting properties, or provide additional interaction with other device layers.
Non-carbazole SAM materials discussed in this chapter were synthesized by utilizing a 3-step synthetic procedure, similar to halogenated carbazole SAM synthesis, discussed in the previous chapter.

Figure 25 Synthesis of phenothiazine and phenoxazine derivatives containing the phosphonic acid group

During the alkylation of phenothiazine and phenoxazine (Figure 25), 4-bromobutyl moiety was introduced, thus obtaining alkylated derivatives **23** and **24**. We chose butyl aliphatic linking group due to better yields, simpler and faster synthesis. By conducting Arbuzov reaction, aliphatic bromide in the formed intermediates was substituted by phosphonic acid ethyl ester to obtain **25** and **26**. Lastly, hydrolysis was performed by utilizing bromotrimethylsilane, resulting in phenothiazine- or phenoxazine-based phosphonic acids **4PAPTZ** and **4PAPOZ**.

To evaluate the energy levels of non-carbazole SAM and compare the obtained results with the already known materials, the ionization potential (I_p) was measured in the solid-state by using the *photoelectron spectroscopy in air* (PESA) method. I_p graphs are presented in Figure 26.

Funded by the European Union
This project has received funding from the European Union's Horizon Europe research and innovation programme under grant agreement No. 101082176

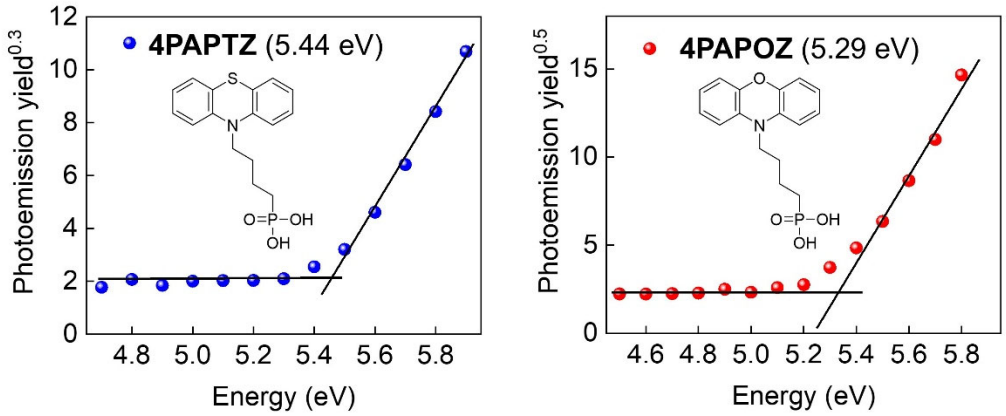

Figure 26 Photoemission in air spectra of SAM derivatives 4PAPTZ, 4PAPOZ.

4PAPTZ and **4PAPOZ** with heteroatom-containing phenoxazine or phenothiazine chromophore demonstrated lower values of I_p specifically, 5.44 and 5.29 eV, which are lower than 2PACz (5.6 eV) and comparable to that of MeO-2PACz (5.3 eV). This information is important for better understanding of how the energy levels can be tuned to the desired value by adjusting the chromophore and substituents in molecules.

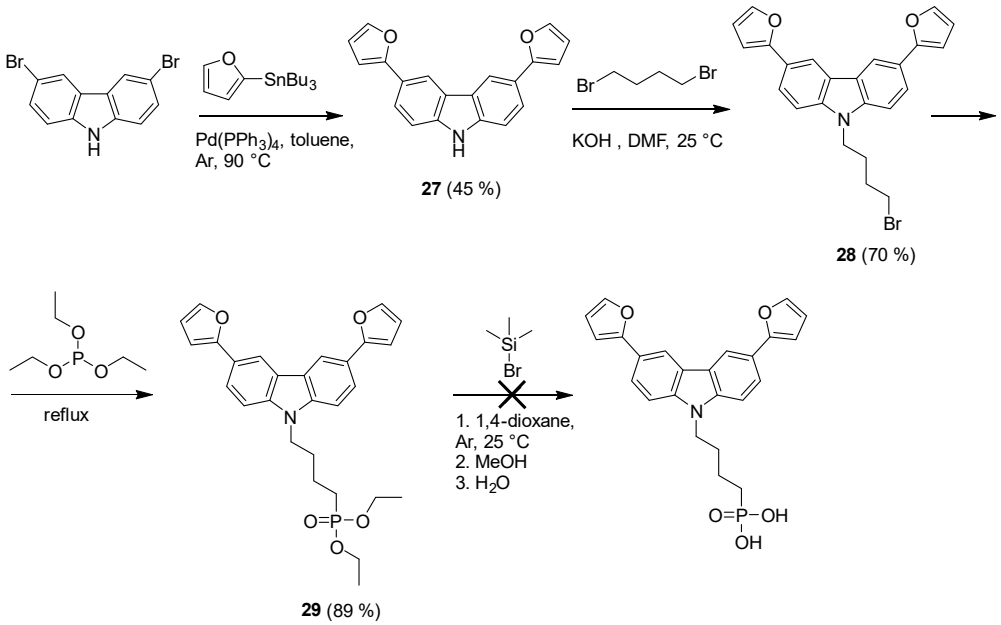

Figure 27 Synthesis attempts to obtain carbazole derivative containing furan and phosphonic acid groups

The addition of furan substituents could be useful for the extension of the conjugated system of carbazole; furthermore, furane moieties could potentially interact with perovskite, similarly as thiophene-containing derivatives. For the introduction of furan substituents (Figure 27), Stille coupling was employed, by using 2-(tributylstannyl)furan and tetrakis(triphenylphosphine)palladium(0) in toluene under argon, resulting in intermediate **27**, which was further alkylated and transformed into a phosphonate derivative, thus obtaining compounds **28** and **29**, respectively. The final step of hydrolysis, however, did not go as planned, as the product was obtained as an insoluble black solid, and its structure could not be determined. This could happen due to the possible condensation of

Funded by the European Union
This project has received funding from the European Union's Horizon Europe research and innovation programme under grant agreement No. 101082176

furans in the presence of hydrobromic acid which is released during the reaction as a side product.

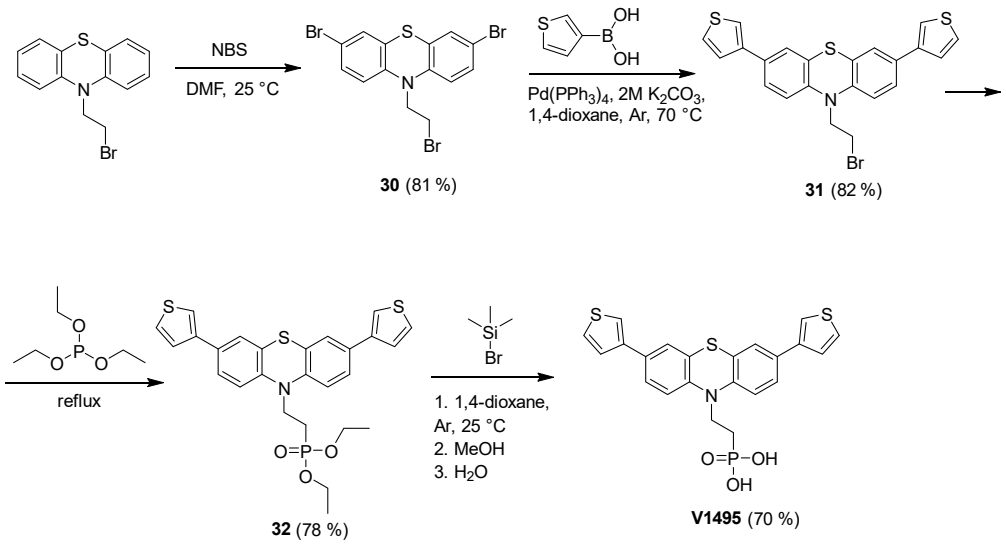

Figure 28 Synthesis of phenothiazine derivative containing thiophene and phosphonic acid groups

Phenothiazine was chosen together with thiophene moieties to provide sulfur heteroatoms in the structure, thus adding some additional interaction between material and perovskite layer. Bromination was conducted using NBS in dimethylformamide (Figure 28). The isolated phenothiazine **30** was used for the palladium catalyzed Suzuki-Miyaura coupling reaction with 3-thienylboronic acid under argon in anhydrous 1,4-dioxane. The obtained intermediate **31** was transformed into the final product **V1495** containing the phosphonic acid group *via* phosphonylation and hydrolysis reactions.
Similarly to the previously discussed materials, the synthesized molecules containing different functional groups and a phosphonic acid group were initially investigated by measuring their ionization potential by the *photoelectron spectroscopy in air* (PESA) method.

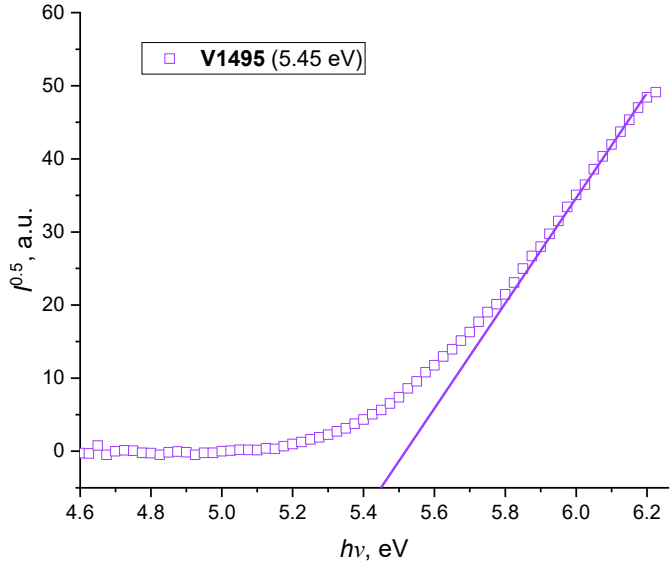

Figure 29 Photoemission in air spectra of SAM derivative V1495

The measurement result is shown in Figure 29. Interestingly, addition of electron donating thiophene

Funded by the European Union
This project has received funding from the European Union's Horizon Europe research and innovation programme under grant agreement No. 101082176

functional groups did not decrease the I_p value, indicating that thiophenes are twisted out of the conjugation plane.
From the results of the primary investigation a series of heterocycles containing functional groups providing additional interaction with perovskite layer (**4PAPOZ**, **4PAPTZ**, **V1495**) were selected (energy levels, ease of synthesis) for further testing in the devices at project partners facilities (WP2, Task 2.1) to determine suitability of this type of materials.

1.7.3. Hole-transporting material suitable for in situ thermal cross-linking

In the case of p-i-n devices, polymeric HTMs, such as poly(3,4-ethylenedioxythiophene):polystyrene sulfonate (**PEDOT:PSS**), poly[3-(4-carboxylatebutyl)thiophene] (**P3CT**) derivatives, and poly[bis(4-phenyl)(2,4,6-trimethylphenyl)amine] (**PTAA**) or combinations thereof, are widely used. Among them, **PTAA**, with its excellent electrical properties and chemical neutrality, has attracted particular interest. However, tedious synthetic process and batch-to-batch variation of **PTAA** remain significant issues restricting its application to large-scale device fabrication. In this regard, small molecular organic molecules offer potential advantages such as a well-defined molecular weight, ease of synthesis, and good reproducibility. The use of molecules with anchoring groups such as phosphonic acid or carboxylic acid, that can spontaneously bind to the transparent conducting oxide surface and form a conformal hole-collecting monolayer, has been demonstrated as an effective way of using small molecules instead. An alternative approach is to polymerize the small molecules in situ via cross-linking reactions. Soluble small molecules bearing cross-linkable units, such as vinyl, acrylate, azide, and oxetane groups, can form insoluble cross-linked 3D networks under thermal or UV treatment. Such cross-linked 3D networks could enable hole-transporting layers and protective interlayers. However, previously the reported cross-linkable systems would not be suitable for flexible p-i-n PSCs with film substrates due to their high crosslinking temperatures (usually > 180 °C), which exceed the tolerance of the underlying layers.
KTU has developed 9,9′-spirobifluorene-based molecule functionalized with four vinyl groups (**V1382**) for the cross-linkable HTL (Figure 30). To lower the cross-linking temperature a cross-linker containing thiol groups 4,4′-thiobisbenzenethiol, was used. Structurally it is relatively small insulating part and may generate a stable radical form to facilitate the thiol-ene reaction with **V1382**.

The polymer precursor **V1382**, which possesses a 9,9′-spirobifluorene core and four vinyl cross-linkable groups, was synthesized in a facile 2-step synthetic procedure with commercially available starting materials as shown in Figure 30. Initially palladium-catalyzed Buchwald–Hartwig amination reaction of 2,2′,7,7′-tetrabromo-9,9′-spirobifluorene and *p*-anisidine was carried out to give aminated precursor in 70% yield. It was then vinyl-functionalized using 4-bromostyrene to generate the target product **V1382** in 51% yield.

Funded by the European Union
This project has received funding from the European Union's Horizon Europe research and innovation programme under grant agreement No. 101082176

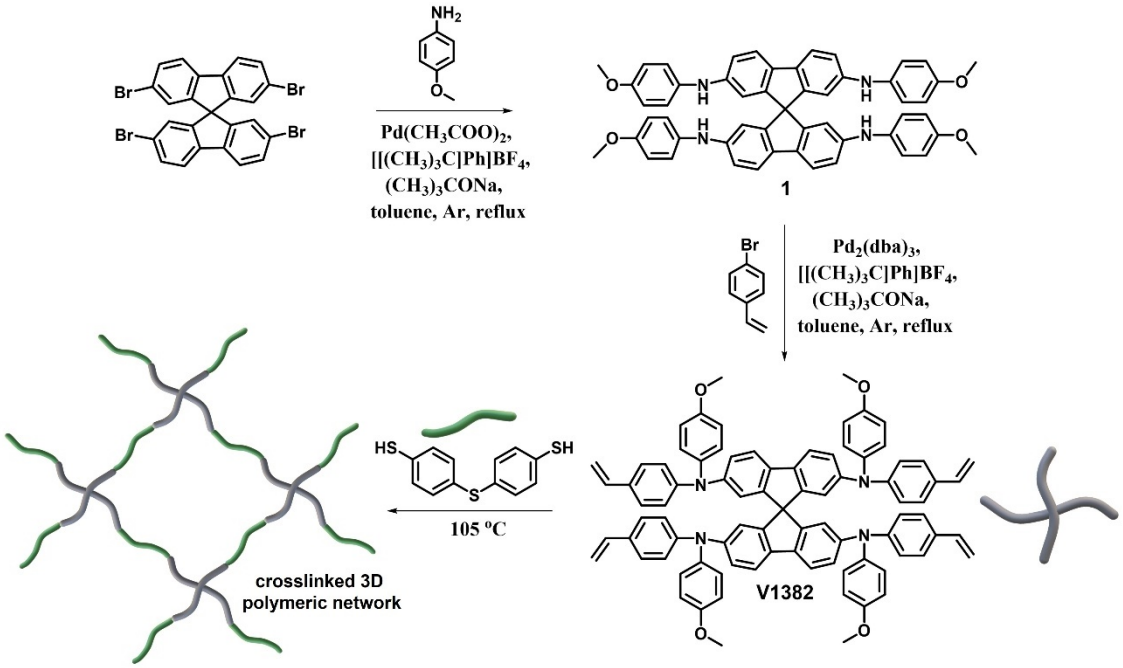

Figure 30 Synthetic route of the 9,9'-spirobifluorene polymer precursor V1382 and its schematic thiol-ene cross-linking using 4,4'-thiobisbenzenethiol as a cross-linker

The thermal properties of **V1382** and its cross-linking reaction with 4,4'-thiobisbenzenethiol were investigated by thermogravimetric analysis (TGA) and differential scanning calorimetry (DSC). The decomposition temperature corresponding to 5% weight loss (T_{dec}) of **V1382** was estimated from the TGA curve to be 460 °C, confirming that **V1382** has good thermal stability. As shown in Figure 31a, an exothermic peak was detected at 253 °C during the first scan, while no distinct phase transition could be observed until 350 °C in the second heating scan, suggesting that thermal cross-linking of **V1382** occurs at 253 °C. In contrast, after mixing **V1382** with a dithiol cross-linker 4,4'-thiobisbenzenethiol, in a molar ratio of 1:2, the exothermic peak shifted to the region of 103–120 °C, and the cross-linking temperature (T_{poly}) was detected at 107 °C (Figure 31b). The results imply that the fast thermal cross-linking occurs due to the facile thiol-ene reaction. It is worth noting that this is the lowest cross-linking temperature reported in the PSC field, enabling the application in both p-i-n and n-i-p PSC architectures.

Funded by the European Union

This project has received funding from the European Union's Horizon Europe research and innovation programme under grant agreement No. 101082176

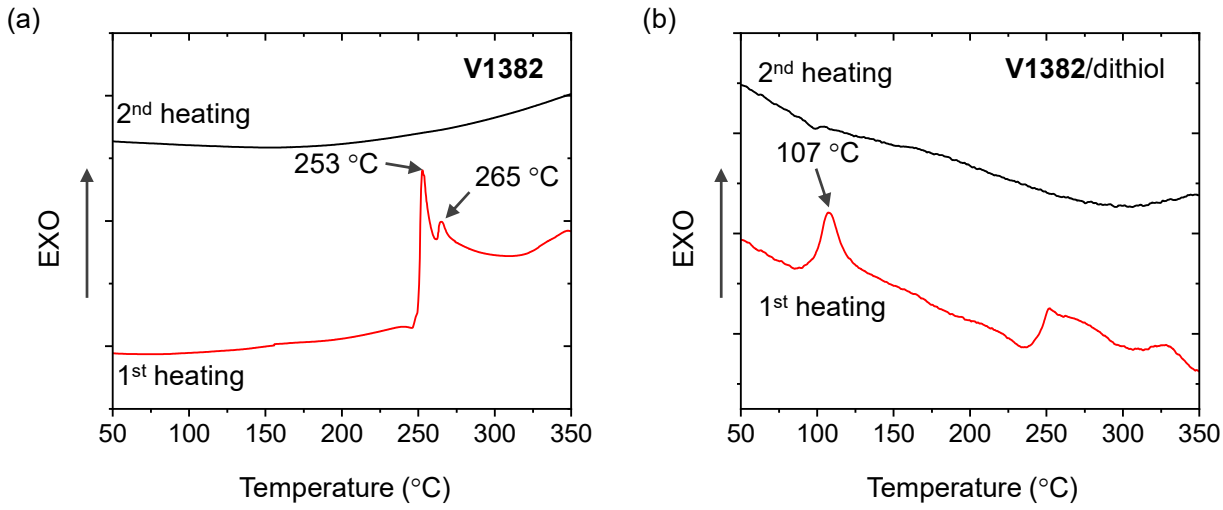

Figure 31 Differential scanning calorimetry curves (scan rate 10 °C min^{-1}, N_2 atmosphere) of (a) V1382 and (b) a mixture of V1382 with 4,4'-thiobisbenzenethiol

To evaluate the light absorbance of **V1382** and formed polymers, ultraviolet–visible (UV–Vis) absorption was measured from tetrahydrofuran (THF) solutions and thin films. The absorption maxima (λ_{abs}) of **V1382** were observed at 336 and 395 nm. The less intense absorption peak at 336 nm can be assigned to the π–π* transition, while the more intense absorption peak at 395 nm corresponds to the n–π* transition, indicating little parasitic absorption by the layer of material.

V1382 films with and without 4,4'-thiobisbenzenethiol cross-linker (molar ratio = 1:2) were prepared by spin-coating the corresponding materials in THF solutions (**V1382** 20 mg mL^{-1}). The ability to form insoluble cross-linked networks was evaluated by measuring the UV–Vis absorption of these spin-coated films. After annealing the films of **V1382** without and with the dithiol cross-linker for 15 minutes at 255 °C and 103 °C, respectively, and rinsing with THF several times to remove soluble parts, absorbance from the films was still detected. It indicates that cross-linking occurred under these conditions, resulting in good solvent-resistant films.

The Fourier-transform infrared (FTIR) spectra (Figure 32) were recorded to ascertain the occurrence of the cross-linking. After **V1382** cross-linking with dithiol at 103 °C, the peak of S–H stretching vibration at 2520 cm^{-1} and the peak of C=C stretching vibration at 1625 cm^{-1} disappeared comparing with the peaks before heating confirming that fast thermal cross-linking occurs after heating **V1382** with a dithiol cross-linker at 103 °C.

Funded by the European Union
This project has received funding from the European Union's Horizon Europe research and innovation programme under grant agreement No. 101082176

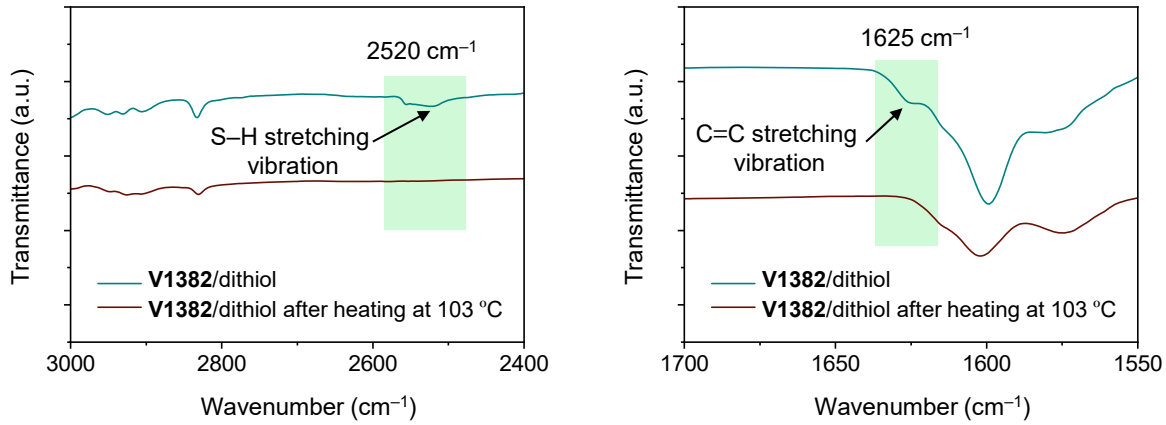

Figure 32 FTIR spectra before and after cross-linking of V1382 with dithiol.

The hole-transporting properties of the HTMs were characterized with the aid of xerographic time-of-flight (XTOF) measurements (Figure 33a). At zero field strength, **V1382** demonstrates a hole drift mobility of 8.7×10^{-5} cm^2 V^{-1} s^{-1}. After thermal annealing, regardless of using the dithiol cross-linker, the hole mobilities of cross-linked films was slightly reduced to 1.3×10^{-5} cm^2 V^{-1} s^{-1}, yet still comparable to those of popular HTMs for PSCs. In addition, the solid-state ionization potential (I_p) of **V1382** and the cross-linked films were measured by using photoelectron spectroscopy in air (PESA). As shown in Figure 33b, the ionization potential of **V1382** film was measured to be 5.29 eV. The I_p values slightly increase to 5.38 and 5.35 eV in the case of cross-linked **V1382** without and with 4,4'-thiobisbenzenethiol, respectively.

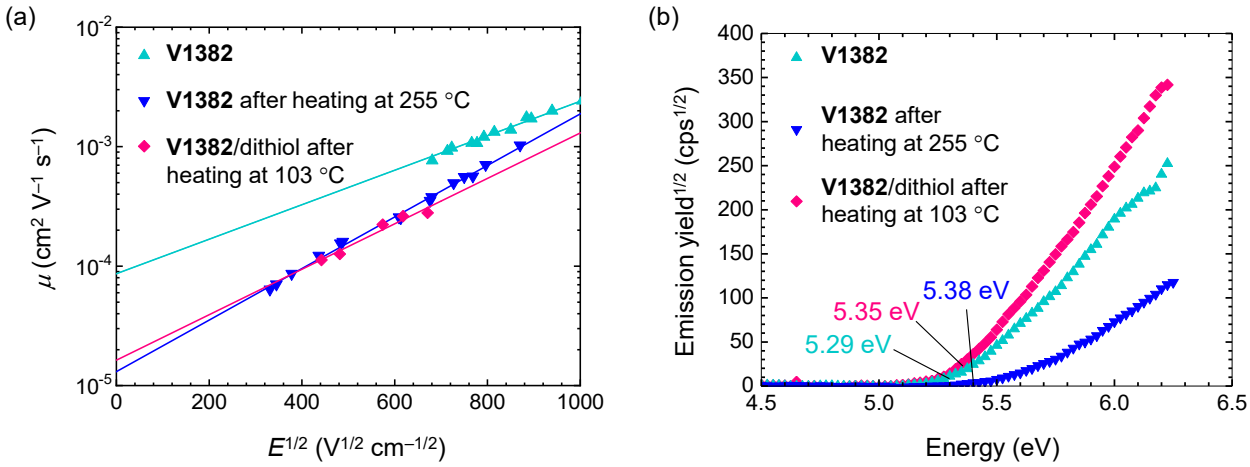

Figure 33 (a) Electric field dependencies of the hole-drift mobilities in charge transport layers and (b) Photoelectron yield of V1382 and cross-linked films measured in air

The X-ray photoelectron spectroscopy (XPS) measurements were carried out to prove the interaction between the cross-linked **V1382**/dithiol and the perovskite ($Cs_{0.05}FA_{0.80}MA_{0.15}PbI_{2.75}Br_{0.25}$). Figure 34 presents the XPS spectra of Pb 4*f* peaks in the pristine perovskite film and the perovskite film with the cross-linked polymer surface modification. Compared to the pristine film, the peaks of Pb $4f_{7/2}$ and Pb $4f_{5/2}$ in the modified perovskite film shifted 0.3 eV to higher binding energy, implying an interaction between the cross-linked **V1382**/dithiol and the perovskite surface. This could benefit solar cell operational stability.

Funded by the European Union
This project has received funding from the European Union's Horizon Europe research and innovation programme under grant agreement No. 101082176

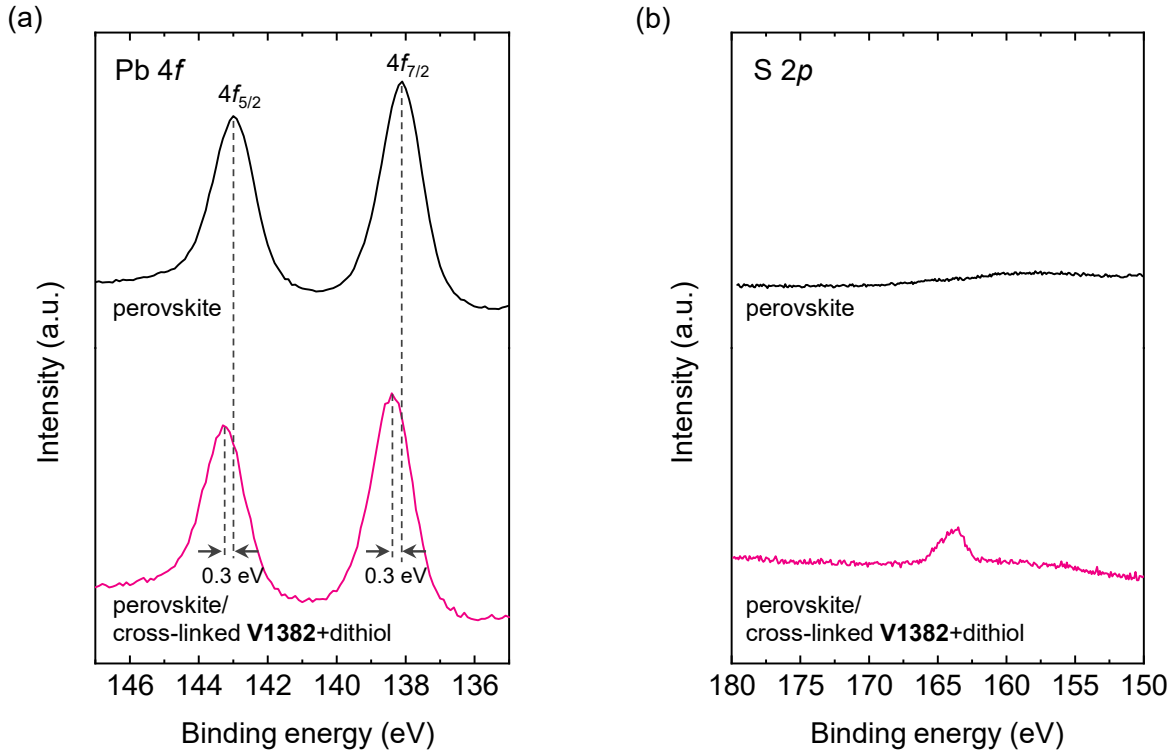

Figure 34 XPS spectra of (a) Pb 4f and (b) S 2p of the pristine perovskite and perovskite coated with cross-linked V1382/dithiol

The concentration of **V1382** used for cross-linking with dithiol was optimized to be 2.0 mg mL^{-1}. Preliminary tests in the PSC devices indicated that cross-linked **V1382**/dithiol film fabricated by using < 2.0 mg mL^{-1} of **V1382** exhibited a lower open-circuit voltage and a larger hysteresis, while those using > 2.0 mg mL^{-1} of **V1382** showed a lower fill factor.

We found that the cross-linking between **V1382** and 4,4'-thiobisbenzenethiol (dithiol) can occur at a low temperature of 103 °C to form an insoluble 3D polymer network. To the best of our knowledge, this is the lowest cross-linking temperature for HTLs reported for PSCs. Benefiting from the mild cross-linking conditions, this system is suitable for applications in both p-i-n and n-i-p PSC architectures. Preliminary tests in the devices employing the cross-linked **V1382**/dithiol as the hole-transporting layer in p-i-n PSCs and as the interlayer between the perovskite layer and **Spiro-OMeTAD** in n-i-p PSCs have shown improved performance and long-term stability compared with devices using conventional HTMs. These results demonstrate cross-linking as an efficient strategy for low-cost and high-performance organic semiconducting materials for photovoltaics.

1.7.4. Asymmetric triphenylethylene-based hole transporting materials

One popular approach to creating efficient HTMs involves modifying the substituents around the central core of spiro or a similar core. Following this approach, HTMs such as X55, SCZF-5, and SFXDAnCBZ have been synthesized, demonstrating PCE of 20.8%, 20.1%, and 20.87%, respectively. Although this strategy has shown promising results in terms of achieving high PCE, it is important to acknowledge its limitations. One significant drawback is the cost and complexity associated with synthesizing the central core used in these materials.

An alternative involves using a less complex central fragment while incorporating substituents known for their strong electron-donating properties. These substituents can be selected to tune the energy levels in the desired direction.

Funded by the European Union
This project has received funding from the European Union's Horizon Europe research and innovation programme under grant agreement No. 101082176

KTU has synthesized new HTMs comprised of triphenylethylene central core and carbazole derivatives as substituents. These materials can be obtained in facile two or three-step synthesis procedure. Triphenylethylene based materials **V1508** and **V1509** were synthesized by palladium cross-coupling reactions between 4,4',4''-(ethene-1,1,2-triyl)tris(bromobenzene) and respective carbazole derivatives (Figure 35).

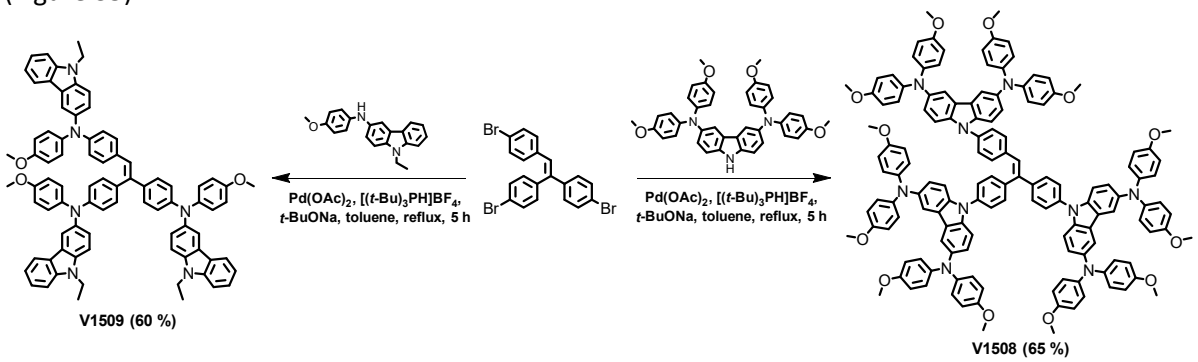

Figure 35 Synthesis of HTMs V1508 and V1509

To determine thermal and morphological stability thermal gravimetric analysis (TGA) and differential scanning calorimetry (DSC) were used. TGA results show that both HTMs are sufficiently stable with decomposition temperatures above 400 °C (Figure 36) which is even more than required for conventional device operation. Analysis of DSC results reveals that triphenylethenyl derivative **V1508** is a molecular glass with glass transition temperature (T_g) of 233 °C, while **V1509** is also amorphous with a lower T_g of 148 °C.

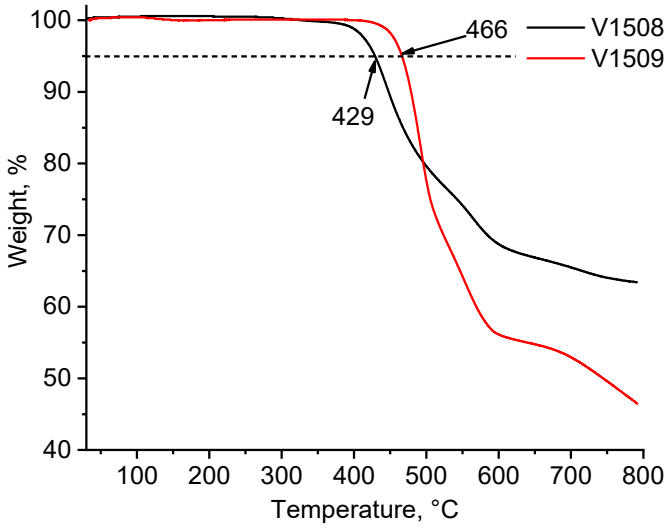

Figure 36 TGA curves of V1508 and V1509.

The UV-visible absorption spectra of the new triphenylethylene derivatives **V1508** and **V1509** have been measured (Table 5, Figure 37). Both materials have similar absorption spectra: they absorb light most intensively at around 300 nm, which corresponds to $\pi-\pi^*$ electron transition, while less intense peaks that can be attributed to n−π* transitions are observed at roughly 380 nm for **V1508** and around 400 nm for **V1509**, indicating little parasitic absorption by the materials layer.

Funded by the European Union
This project has received funding from the European Union's Horizon Europe research and innovation programme under grant agreement No. 101082176

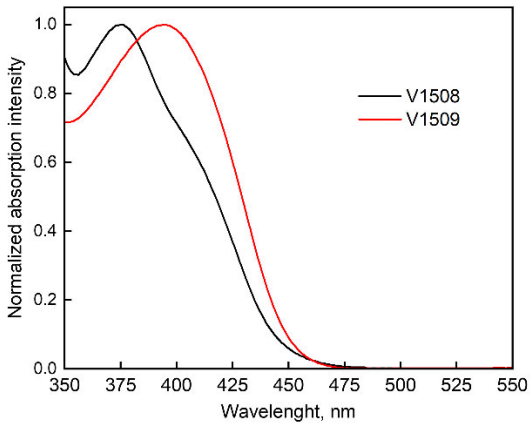

Figure 37 UV-Vis absorption spectra of HTMs V1508 and V1509 in the film

To evaluate the compatibility of the new HTMs with the perovskite ionization potential (I_p) was measured by the photoelectron spectroscopy in the air (PESA) method (Figure 38a). From the results, triphenylethylene derivatives **V1508** and **V1509** possess the necessary energy levels needed for the transfer of holes from the perovskite towards the electrode (Table 5). It is also worth noting that although both HTMs have suitable energy levels, **V1508** has slightly higher I_p value (by 0.11 eV) which might result from more steric hindrance occurring due to the larger molecule size compared to **V1509**.

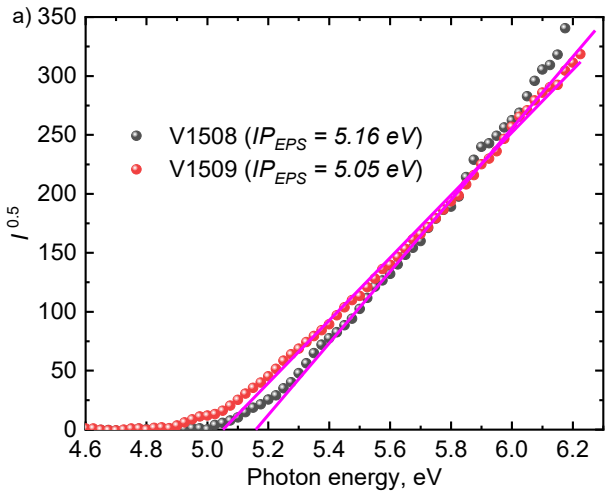

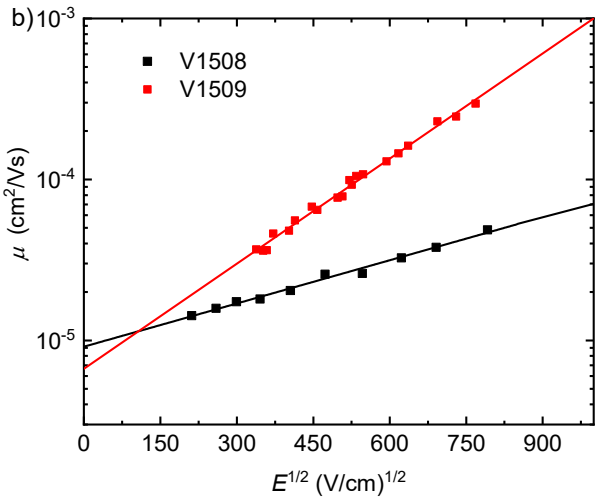

Figure 38 (a) Ionization potential; (b) hole-drift mobility of V1508 and V1509

The hole mobility was measured from films by the xerographic time-of-flight (XTOF) method with the electric field dependencies of the hole-drift mobility shown in Figure 38b. Mobility at zero field strength (μ_0) of new HTMs **V1508** and **V1509** was determined to be $9.1 \cdot 10^{-6}$ cm^2 V^{-1} s^{-1} and $6.6 \cdot 10^{-6}$ cm^2 V^{-1} s^{-1} respectively, demonstrating that in this case, the size of substituents around triphenylethylene have little effect on the speed of charge extraction.

Table 5 Thermal, Optical, and Photophysical Properties of the Synthesized Materials

ID	T_g, °C	T_{dec}, °C	λ_{abs}, nm	I_p, eV	μ_0, cm^2 V^{-1} s^{-1}
V1508	233	429	307, 375	5.16	$9.1 \cdot 10^{-6}$
V1509	148	466	304, 393	5.05	$6.6 \cdot 10^{-6}$

Developed hole transporting materials were obtained *via* straightforward synthetic procedure and demonstrate suitable characteristics for application in PSCs. A crucial advantage of these HTMs is their lower cost, making them promising candidates for practical applications in the field of solar energy conversion.

1.8. Electron transporting materials

In the perovskite solar cells field, the most widely used n-type semiconductors for photoelectron extraction are fullerene and its functionalized derivative $PC_{61}BM$. The reasons for its dominance are twofold, on one hand these materials demonstrate good performance in the devices, on the other hand there is scarcity of suitable acceptor alternatives for non-fullerene ETMs synthesis. C_{60} and its derivatives have their own drawbacks, however, chief among them are relatively expensive and quite complicated synthesis, difficulty of chemical modification and poor adhesion of the formed layers which causes delamination. The poor choice of non-fullerene n-type semiconductors demonstrating good photovoltaic characteristics in PSC encourages us to delve deeper into this problem, looking for simpler to make, less expensive alternatives to C_{60}, thus moving closer to commercialization of the PSC technology.

1.8.1. 1,4,5,8-Naphthalene tetracarboxylic diimide-based electron transporting materials

Among non-fullerene alternatives, naphthalene tetracarboxylic diimide (NDI)-based small molecules

Funded by the European Union
This project has received funding from the European Union's Horizon Europe research and innovation programme under grant agreement No. 101082176

offer favorable n-type semiconductor properties, such as high electron affinity, electron mobility, and photochemical stability, coupled with simple synthesis [1]. One of the first symmetric NDI compounds containing carboxylic functional group demonstrated sufficiently high device characteristics, reaching 16 % efficiency and 70 % fill factor in n-i-p perovskite solar cells [2], thus motivating us to design new electron transporting materials based on NID core in WP1 Task 1.2 and test them in WP2 Task 2.1 of the VALHALLA project.
Apart from suitable semiconducting characteristics another point we must address while designing these materials is poor adhesion between layers. To combat this problem, we propose introduction of the functional groups (such as phosphonic acids and esters) which would interact with the layers above and below ETL, namely perovskite and SnO2. Finally, project foresees investigation of both wet and dry deposition methods, therefore we aim to develop materials which would be suitable for such applications. In particular, development of the molecules capable of forming films *via* vacuum deposition is not a trivial task as moieties inhibiting delamination would also make materials more difficult to sublime due to intermolecular interactions, therefore fine balance is needed.

The synthesis of NDIs containing the phosphonic acid group is shown in Figure 46.. By using one-pot condensation of 1,4,5,8-tetracarboxylic dianhydride with diethyl(aminomethyl)phosphonate and 2,5-di-*tert*-butylaniline intermediate **33** was isolated. The obtained phosphonate ester **33** was hydrolyzed by using either bromotrimethylsilane in 1,4-dioxane or *via* refluxing in concentrated hydrochloric acid to obtain NDI derivative **PANDI** containing a phosphonic acid functional group. It should be noted that the second method, which uses hydrochloric acid, provided a better yield (95 %).

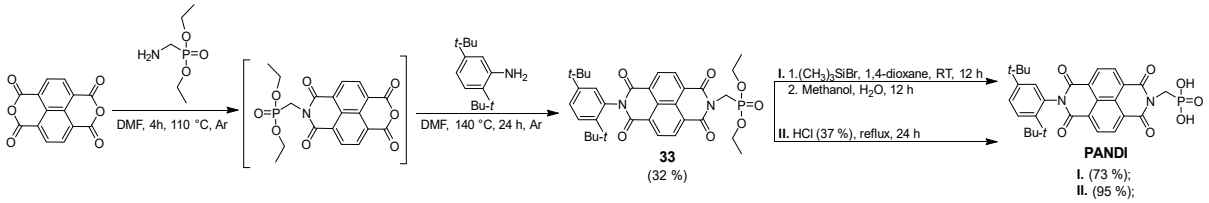

Figure 39 Synthesis of 1,4,5,8-naphthalene diimide derivative PANDI.

The suitability for application of the synthesized materials in perovskite solar cells was analyzed by investigating their electrochemical properties and thermal stability. Thermogravimetric analysis measurements proved that semiconductor **PANDI** is sufficiently thermally stable for their application in photovoltaic devices (Figure 40). It lost 5% of their mass at 395 °C. Although in the TGA profile rapid weight loss, indicating evaporation, is quite small, thus vacuum deposition could be difficult.

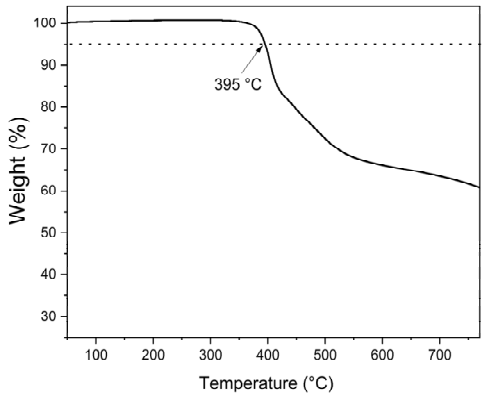

Figure 40 TGA curve of PANDI

In the UV-Vis spectrum, absorption bands appear in the range of 340–385 nm, and can be attributed

Funded by the European Union
This project has received funding from the European Union's Horizon Europe research and innovation programme under grant agreement No. 101082176

to the π-π* transitions of the naphthalene diimide chromophore (Figure 41). The second absorption peak (at 217nm and 236 nm) is due to the n-σ* transition involving also a 2,5-di-*tert*-butylphenyl fragment. UV-Vis spectrum indicates very little absorption in the visible range of the spectrum, thus material shouldn't diminish performance of the device due to parasitic absorption.

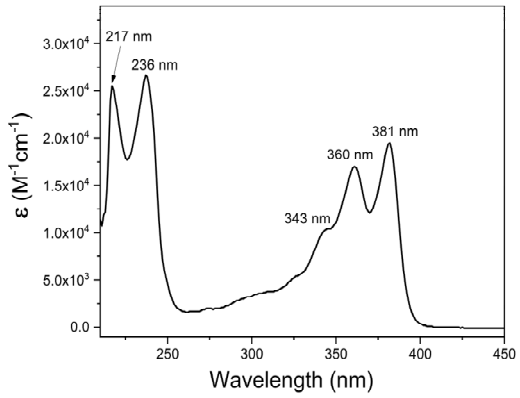

Figure 41 UV-Vis spectra of PANDI in $CHCl_3$ solution ($c=10^{-4}$ M)

The redox potential of the NDI derivative was measured by employing cyclic voltamperometry. These values were used to compare different compounds in relation to one another.

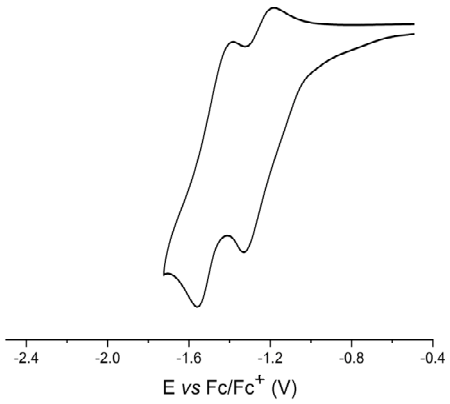

Figure 42 Redox voltamperogram of PANDI

The voltammogram of ETM **PANDI** in the solution show two quasi-reversible reduction waves during the scans and are typical for naphthalene diimide derivatives (Figure 42). The reversible process indicates that all materials exhibit good electrochemical stability. The E_{LUMO} level was calculated to be -3.8 eV, while the E_{HOMO} level was -6.9 eV.

The discussed naphthalene diimide, containing one phosphonic acid anchoring group, and synthesized *via* one-pot condensation followed by the McKenna reaction or hydrolysis under acidic conditions was preliminary tested in the PSC devices to assess suitability of this approach. NDI **PANDI** has been successfully applied as an electron-selective monolayer for n-i-p perovskite solar cells. It was found that an increase in the surface homogeneity of ITO/**PANDI**/perovskite can effectively suppress the non-radiative interfacial recombination through the perovskite passivation effect. In this suitability investigation an ITO/NDI **PANDI** base n-i-p perovskite solar cell demonstrated an efficiency of 21.5%. Additionally, it was determined that NDI SAMs are suitable for application with flexible substrates (e.g.,

Funded by the European Union
This project has received funding from the European Union's Horizon Europe research and innovation programme under grant agreement No. 101082176

ITO-PET). After these successful tests in n-i-p setup, it was decided that proposed approach for design of electron selective materials is interesting enough to transfer the idea to the p-i-n devices, albeit with modification to the structure, to suit more fully the needs of this project.

Therefore, symmetric naphthalene diimide with phosphonic acid substituents was synthesized by treating 1,4,5,8-napthalenetetracarboxylic dianhydride with the relevant alkylamines at reflux in acetic acid under argon atmosphere for 12–48 hours (Figure 43). The phosphonate hydrolysis of intermediates **V1657** and **V1792** was conducted in a similar manner as mentioned in previously, i.e. by using the McKenna method or hydrolysis under acidic conditions. The second synthesis method using concentrated hydrochloric acid provided better yield (96% and 93% respectively).

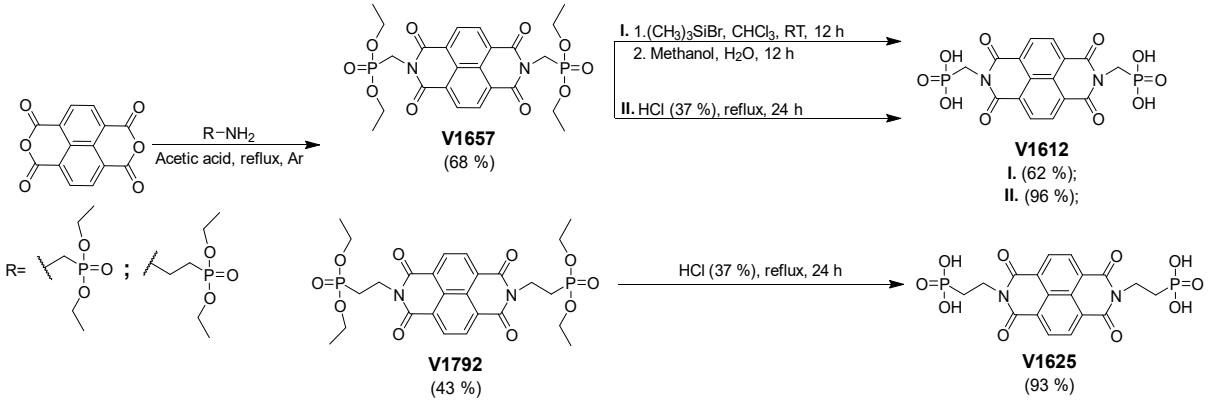

Figure 43 Synthesis of symmetric 1,4,5,8-naphthalene diimide derivatives V1612, V1625

Similar material containing Br atoms attached to the central naphthalene core was synthesized in order to get deeper LUMO energy levels. Naphthalene diimide **V1486** was obtained in two steps via intermediate ester **V1568** under similar reaction conditions to those discussed earlier (Figure 44).

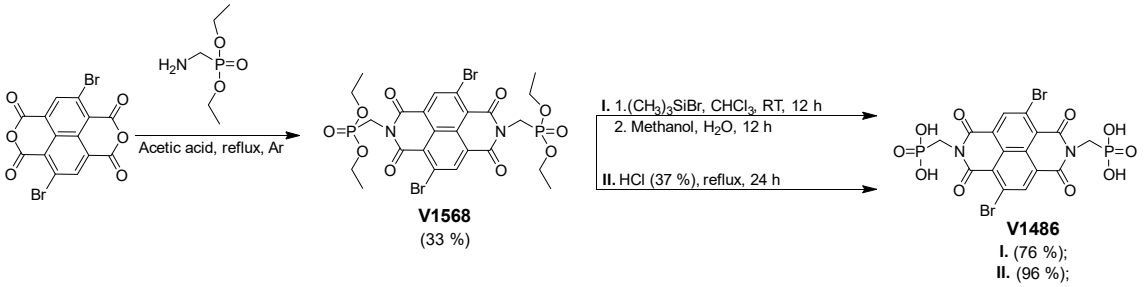

Figure 44 Synthesis of 1,4,5,8-naphthalene diimide derivative V1486

Semiconductors **V1486**, **V1612**, **V1625** showed good thermal stability with 5% weight loss within the temperature range of 326–483 °C (Table 6). TGA example is shown in Figure 45, from the profile of the curve we can see that some rapid weight loss occurs above 400 °C, thus indicating evaporation of the material, although temperature range is somewhat narrow, as after certain point evaporation is superseded by slow going decomposition.

Table 6 Thermal properties of NDIs V1486, V1612, V1625

Compound No.	Structure	T_{dec}, °C
V1612		483
V1625		434

Funded by the European Union
This project has received funding from the European Union's Horizon Europe research and innovation programme under grant agreement No. 101082176

V1486		438

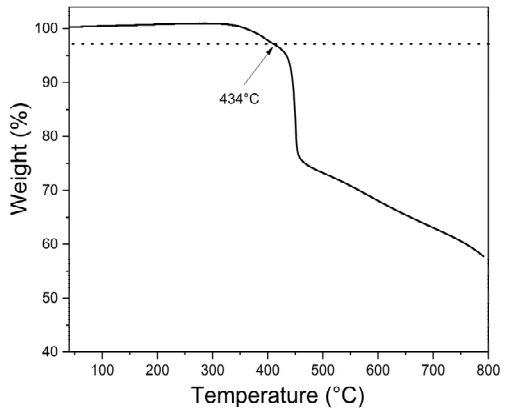

Figure 45 TGA curve of NDI V1625

After investigation of the synthesized molecules at the project partners facilities the synthesized symmetric materials demonstrated reasonable suitability for vacuum deposition. In hope to improve sublimability esters **V1657** and **V1792**, which had better TGA profiles, were also delivered to project partners for investigation. Unfortunately, they did not demonstrate necessary interaction with other layers.

Partially hydrolized phosphonic ester was synthesized in hopes that both solubility and sublimability will improve as interactions between molecules will be weakened, however by keeping one OH group on each side, we hoped that those interactions will not be diminished to the level of ester molecule.

As depicted in Figure 46, symmetric naphthalimide with a partially hydrolyzed phosphonic ester was synthesized *via* a two-step reaction. Naphthalene intermediate **34** was prepared by the condensation of 1,4,5,8-napthalenetetracarboxylic dianhydride with diethyl(2-aminoethyl)phosphonate at reflux in acetic acid under an argon atmosphere for 48 hours. The phosphonate intermediate was then hydrolyzed using sodium azide in DMF at 100 °C for 36 hours, followed by the acidification of the reaction mixture with concentrated HCl to a pH 1 to afford compound **V1766**.

Funded by the European Union

This project has received funding from the European Union's Horizon Europe research and innovation programme under grant agreement No. 101082176

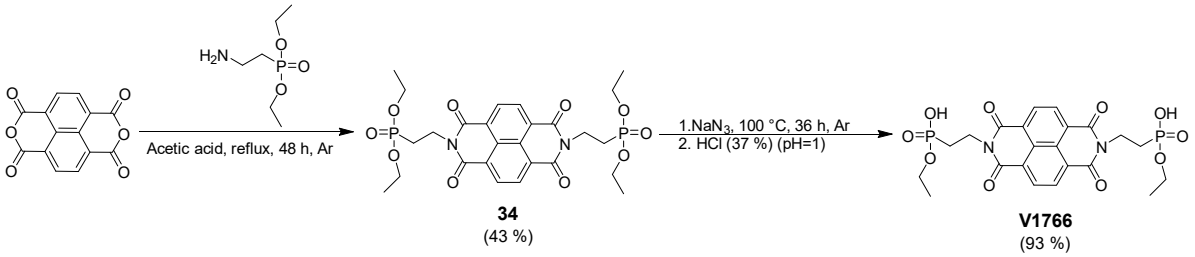

Figure 46 Synthesis of naphthalene diimide V1766

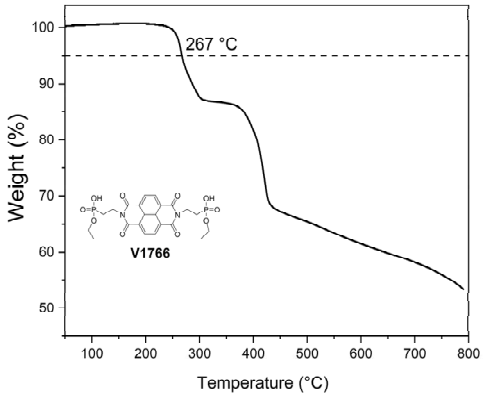

Figure 47 TGA curve of naphthalene diimide V1766

V1766 demonstrated similar TGA profile (Figure 47) to the **V1625**, although not as steep which was somewhat unexpected as it was envisioned that partial hydrolysis would limit amount of intermolecular interactions and make material easier to evaporate.

The compounds **V1486**, **V1612**, **V1625** exhibited quasi-reversible reduction waves. The reversible process indicates that the materials exhibit good electrochemical stability. The LUMO/ HOMO energy levels of ETMs **V1486**, **V1612**, **V1625** were calculated to be in the ranges from -3.63 eV to -3.9 eV and from -6.53 eV to -7.06 eV, respectively (Table 7).

Table 7 Electrochemical andoprical characteristics of symmetric NDIs

Compound	E_{HOMO}, [eV]	E_{LUMO}, [eV]	λ_{abs}, [nm]	$E_g^{opt-sol}$, [eV]
V1612	-6.97	-3.9	403	3.07
V1625	-6.91	-3.79	397	3.12
V1486	-6.76	-3.86	426	2.90

Light absorption of the synthesized materials was investigated using UV-Vis spectroscopy. The spectra indicate that light absorption takes place in the UV region, with three maxima at 341 nm, 360 nm and 380 nm, which are attributed to the π-π* transitions of the chromophore core. The band gap of semiconductors **V1486**, **V1612**, **V1625** was estimated from the edges of the electronic absorption spectra to be between 2.88 and 3.16 eV (Table 7).
From the results of the primary investigation a series of NDIs containing functional groups capable of interaction with perovskite and SnO2 layers (**PANDI**, **V1486**, **V1612**, **V1625**, **V1657**, **V1658**, **V1766**) were selected for further testing in the devices at project partners facilities (WP2, Task 2.1) to determine suitability of this type of materials.

Funded by the European Union
This project has received funding from the European Union's Horizon Europe research and innovation programme under grant agreement No. 101082176

1.8.2. Asymmetric perinone-based electron-collecting monolayer materials

In general, there isn't a wide variety of compounds suitable for use as electron transporting materials. And even among those that are available good portion requires relatively complex multistage synthesis.

In our research, KTU has concentrated on perinone structure as a potential electron-collecting material. Perinone derivatives have potential to become attractive n-type semiconducting materials for organic electronic devices due to their high electron affinity. The perinone structure is known for its inherent stability, a desirable trait for ETMs in PSCs that need to withstand operational stresses like heat and prolonged light exposure, contributing to the long-term operational stability of the solar cell. Additionally, perinone derivatives can be chemically modified to fine-tune their HOMO and LUMO energy levels. Thus, achieving an optimal energy level alignment with the perovskite, facilitating efficient electron injection from the perovskite to the ETM and minimizing energy losses.

Synthesis of the perinone derivatives is shown in Figure 48 Synthesis of asymmetric perinone-based molecules. The phosphonate ester precursor compounds **35**–**40** were synthesized *via* a one-pot synthesis protocol consisting of a condensation reaction of naphthalene-1,4,5,8-tetracarboxylic dianhydride and corresponding substituted *o*-phenylenediamine derivatives, followed by the imidation reaction with diethyl(aminomethyl)phosphonate. The synthesis of compounds **35**–**39** was caried out in dry dimethylformamide. However, it was observed that compound **40** undergoes decomposition when DMF is utilized as the reaction solvent. Consequently, for its synthesis, DMF was substituted with glacial acetic acid. The acidic hydrolysis of the phosphonate esters **35**–**39** with concentrated hydrochloric acid at reflux gave the non-substituted **PERNI-H** and substituted **PERNI** derivatives **PERNI-CH3**, **PERNI-F**, **PERNI-Cl**, and **PERNI-Br**. In the case of cyano-substituted **PERNI-CN**, milder hydrolysis conditions were applied using bromo trimethylsilane at room temperature to prevent any side reactions that may occur at the –CN group.

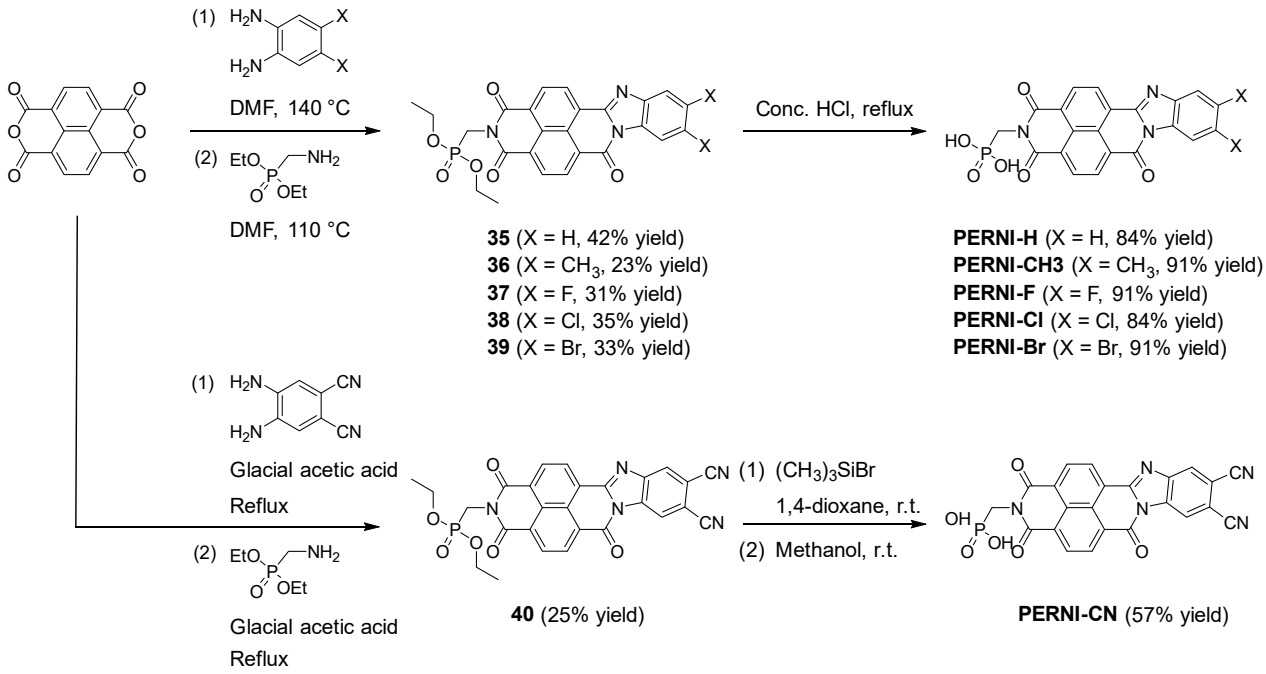

Figure 48 Synthesis of asymmetric perinone-based molecules

Thermal stability of the perinone derivatives was evaluated by thermogravimetric analysis (Figure 49 TGA thermograms of (a) PERNI-H, PERNI-CH3, and PERNI-CN, and (b) PERNI-F, PERNI-Cl, and PERNI-Br at a scan rate of 10 °C min^{-1} under a nitrogen atmosphere). The measurements were carried out under a nitrogen atmosphere at a scan rate of 10 °C min^{-1}. The temperature corresponding to 5% weight loss

Funded by the European Union
This project has received funding from the European Union's Horizon Europe research and innovation programme under grant agreement No. 101082176

(T_{d5}) of the perinone derivatives was estimated to be in the order of **PERNI-CN** (228 °C) < **PERNI-Cl** (294 °C) < **PERNI-H** (326 °C) < **PERNI-Br** (337 °C) < **PERNI-F** (410 °C) < **PERNI-CH3** (453 °C).

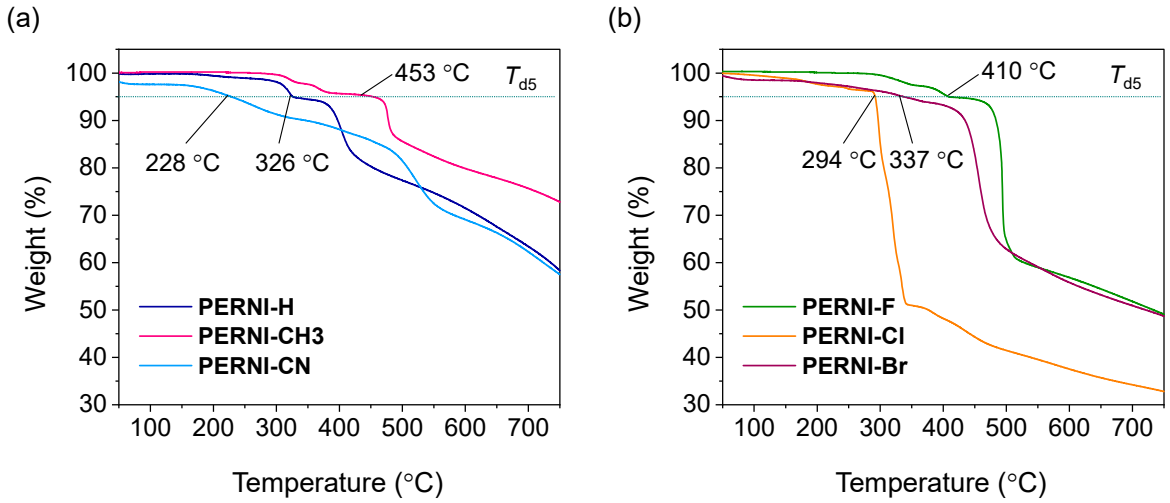

Figure 49 TGA thermograms of (a) PERNI-H, PERNI-CH3, and PERNI-CN, and (b) PERNI-F, PERNI-Cl, and PERNI-Br at a scan rate of 10 °C min^{-1} under a nitrogen atmosphere

Unfortunately, majority of the materials aren't suitable for vacuum deposition as in most of the cases TGA profiles don't show a steep drop in weight, which would be a good indication of rapid evaporation of the material. And even when more pronounced step is observed, the rapid weight loss exhibited by the halogen-substituted perinone derivatives, including **PERNI-F**, **PERNI-Cl**, and **PERNI-Br**, can be ascribed to the release of the halogen atoms. In summary, synthesized perinone derivatives exhibit adequate thermal stability for perovskite solar cell device fabrication by solution process, which is typically conducted at temperatures below 150 °C.

In order to investigate the influence of the substituted functional groups on the photophysical properties, the ultraviolet–visible (UV–Vis) absorption of the perinone derivatives were measured in dimethylacetamide (DMA) solution. The data are presented in Figure 50 UV–Vis absorption spectra in DMA solution 10–4 M of the phosphonic acid group containing perninone derivatives. All compounds exhibit two major absorption bands within the range of 300–325 nm and 400–455 nm, respectively. The broad and intense absorption peak in the longer wavelength region can be attributed to $\pi \rightarrow \pi^*$ transitions. In comparison to non-substituted **PERNI-H** with exhibited a maximum absorption peak (λ^{Ab}_{max}) observed at 433 nm, perinone derivatives with electron-accepting groups demonstrated a hypsochromic shift of 7–20 nm (λ^{Ab}_{max} = 426, 422, 426, and 413 nm for **PERNI-F**, **PERNI-Cl**, **PERNI-Br**, and **PERNI-CN**, respectively). Conversely, a discernible bathochromic shift of 22 nm was evident in the derivative bearing the electron-donating methyl substituent (**PERNI-CH3**, λ^{Ab}_{max} = 455 nm). Overall, materials absorb the light in the visible region somewhat, which could result in some efficiency losses in the PSC devices. Although, usually electron transporting layers aren't very thick (10-20 nm), thus losses shouldn't be too dramatic.

Funded by the European Union
This project has received funding from the European Union's Horizon Europe research and innovation programme under grant agreement No. 101082176

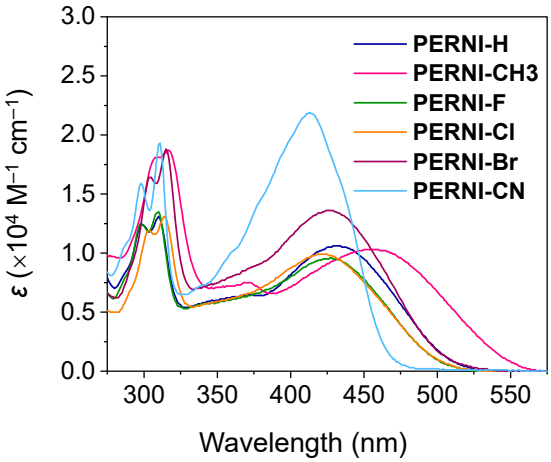

Figure 50 UV–Vis absorption spectra in DMA solution 10–4 M of the phosphonic acid group containing perninone derivatives

Cyclic voltammetry of the compounds reveals quasi-reversible first reduction waves, indicating good electrochemical stability. The half-wave reduction potential ($E_{1/2red}$ vs Fc/Fc^+) of **PERNI-H**, **PERNI-CH3**, **PERNI-F**, **PERNI-Cl**, **PERNI-Br**, and **PERNI-CN** was estimated to be –1.01, –0.84, –0.75, –1.10, –0.95, and –0.92 V, respectively. The LUMO energy levels (E_{LUMO}) were calculated to be –4.09, –4.26, –4.35, –4.00, –4.15, and –4.18 eV for **PERNI-H**, **PERNI-CH3**, **PERNI-F**, **PERNI-Cl**, **PERNI-Br**, and **PERNI-CN**, respectively, by using the following equation: $E_{LUMO} = -(5.1 + E_{1/2red\ vs\ Fc/Fc^+})$, where 5.1 eV is the vacuum energy level of ferrocene. Furthermore, the HOMO levels of these perinone derivatives were estimated to be in the range from –6.50 to –6.89 eV.

Table 8 Electrochemical properties of PERNI derivatives obtained from CV and UV–Vis measurements

Compound	$E_{1/2red\ vs\ Fc/Fc^+}$ [V]	E_{LUMO} [eV]	E_{HOMO} [eV]
PERNI-H	–1.01	–4.09	–6.55
PERNI-CH3	–0.84	–4.26	–6.50
PERNI-F	–0.75	–4.35	–6.91
PERNI-Cl	–1.10	–4.00	–6.62
PERNI-Br	–0.95	–4.15	–6.69
PERNI-CN	–0.92	–4.18	–6.89

In summary, synthesized asymmetric perinone derivatives bearing different substituents (methyl, fluoro, chloro, bromo, and cyano) on the benzimidazole moiety and phosphonic acid group demonstrate sufficient thermal stability, however their TGA profiles indicate that those materials are more suitable for deposition from solution. Presence of suitable frontier molecular orbital energy levels suggests their potential to function as electron-collecting materials in PSCs.
Preliminary investigation of perinone-based compounds was done in n-i-p PSC, materials were used as monolayers. Type of the substituent at benzimidazole moiety has marked influence on the overall device stability, mainly contributing to the better coverage and quality of the perovskite films on the **PERNI**-based monolayers. In this configuration moderate but encouraging results (PCE=10-12%) were obtained. With these preliminary tests we demonstrate that perinones do have potential as electron selective materials, however further research is necessary for their application in p-i-n architecture PSC devices, namely improvement in solubility for wet deposition as currently they are soluble in strongly polar solvents not compatible with perovskite layer.

1.8.3. Anthraquinone-based electron transporting material

Funded by the European Union
This project has received funding from the European Union's Horizon Europe research and innovation programme under grant agreement No. 101082176

In the search for alternative options for electron-selective materials, anthraquinone (AQ) derivatives could be an interesting choice. The AQ structure contains two electron-accepting carbonyl functional groups, which can increase electron affinity and can be easily tuned *via* molecule engineering. Recently, AQ derivative 1-((3-(dimethylamino)propyl)amino)anthracene-9,10-dione was utilized in organic solar cells as an interface modification layer of SnO_2, enhancing the conductivity of the electron-selective contact stack and improving the energy level alignment with the organic photoactive layers. Additionally, AQ derivatives are relatively unexplored as electron transporting materials. Inspired by these results, we explored the possibility of using an AQ moiety in electron-selective materials. We have introduced phosphonic acid functional group to enhance interaction with the neighboring layers.

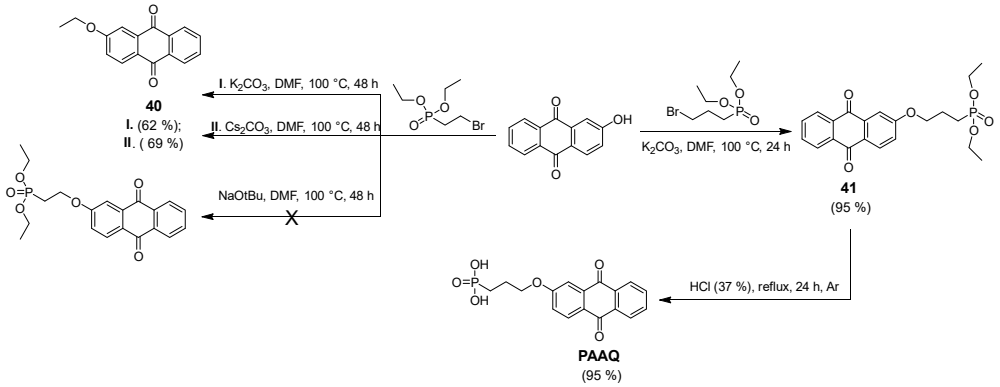

Figure 51 Synthesis of anthraquinone derivatives 41 and PAAQ

Initially, it was attempted to synthesize an anthraquinone derivative with an ethylene bridge connecting the phosphonic acid fragment to the central core, for this task diethyl(2-bromoethyl)phosphonate was employed (Figure 51). 2-Hydroxyanthracene-9,10-dione alkylation using K_2CO_3 or Cs_2CO_3 as the base was unsuccessful; during the first synthesis step, 2-ethoxyanthraquinone (**40**) was obtained instead of the target product (Figure 51). Synthesis of the target intermediate was attempted *via* use of stronger base sodium *tert*-butoxide. Unfortunately, the target product was not obtained, either.

Therefore, it was decided to use a longer propylene aliphatic chain. Anthraquinone-based propylphosphonic acid was synthesized in a two-step procedure from 2-hydroxyanthracene-9,10-dione, which was alkylated with diethyl(3-bromopropyl)phosphonate to give phosphonic ester intermediate **41**. Hydrolysis of the ester groups was carried out under acidic conditions and phosphonic acid **PAAQ** was isolated.

Funded by the European Union

This project has received funding from the European Union's Horizon Europe research and innovation programme under grant agreement No. 101082176

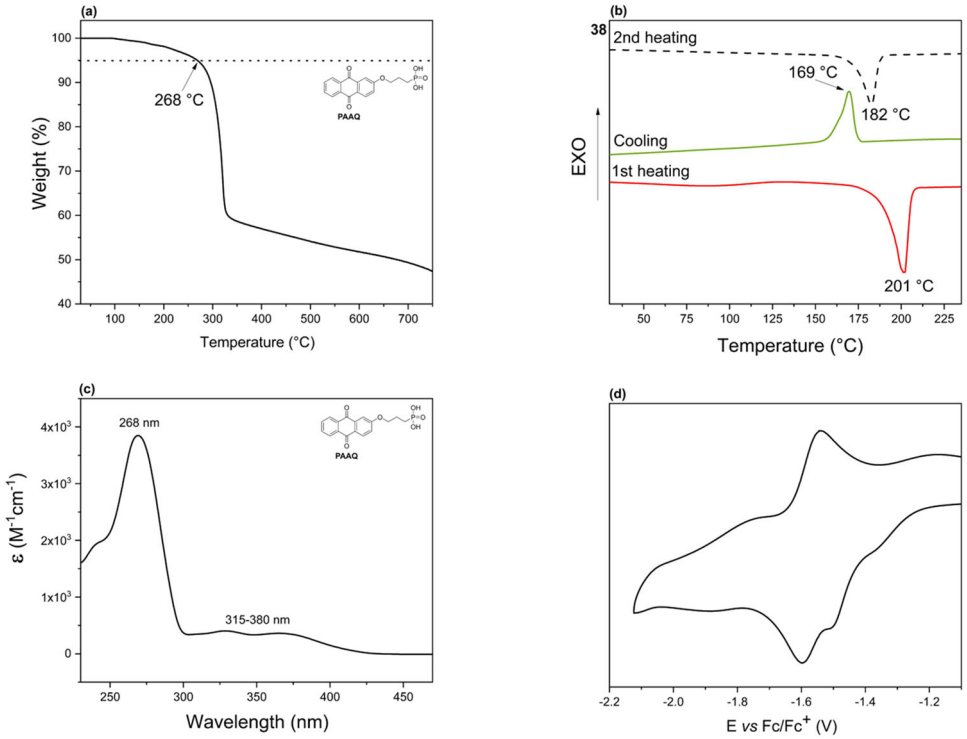

Figure 52 Thermal, optical and electrochemical properties of PAAQ: (a) TGA, (b) DSC curves, (c) UV-Vis spectrum in DMF solution (c=10^{-4} M), (d) redox voltamperogram

Possibility for the application as an n-type semiconductor was analyzed by investigating the optical and electrochemical properties, additionally thermal stability was also investigated. **PAAQ** loses 5% of its weight at 268 °C (Figure 52a), thus demonstrating that it is sufficiently thermally stable. Interestingly, relatively rapid weight loss was observed in the TGA profile, indicating potential for vacuum deposition of the material. During DSC analysis on first heating, endothermic transition is seen at 201 °C, while, upon cooling, an exothermic transition occurs at 169 °C, thus indicating melting and crystallization of the material. During the second heating, only the melting of the material is observed, which indicates that **PAAQ** is fully crystalline (Figure 52b). The DSC curves show that the melting point decreases by 19 °C after first heating and subsequent cooling, thus indicating that **PAAQ** crystallizes into a different crystalline form.
Light absorption maxima of the **PAAQ** were observed at 268 nm and in the 315–380 nm region. These absorption peaks can be assigned to the π-π* and n-π* transitions accordingly (Figure 52c). The band gap for **PAAQ** was calculated to be 3.27 eV. The redox potential of the AQ molecule was measured by employing cyclic voltammetry to determine E_{LUMO} and E_{HOMO} levels. These values do not represent any absolute solid-state electron affinity or ionization energies but can be used to compare different compounds in relation to one another. The voltammogram of the **PAAQ** in a solution shows a quasi-reversible reduction wave during the scans (Figure 52d), demonstrating good electrochemical stability. The calculated E_{LUMO} level for **PAAQ** is -3.52 eV, while E_{HOMO}= -6.79 eV. The redox properties and energy levels of the **PAAQ** are close to those of naphthalene derivatives, thus indicating the potential for use in electron selective layer.

PAAQ shows sufficient thermal stability, suitable energy levels to warrant preliminary investigation as an electron-selective material in PSC. Before transferring it to the project partners we have investigated its electron selectivity in somewhat simpler n-i-p architecture devices as a monolayer. The intermolecular interaction with the other functional layers allowed for formation of broad boundaries

Funded by the European Union
This project has received funding from the European Union's Horizon Europe research and innovation programme under grant agreement No. 101082176

of perovskite grains, reduced morphological defects, and provided sufficiently efficient electron-selective contact at the ITO/perovskite interface. The n-i-p devices achieved efficiency of 17.8%, thus demonstrating potential of anthraquinone derivatives to be utilized as ETM materials.

1.8.1. SnO_2 deposited with pulsed laser deposition

SnO_x thin films were deposited for being used as electron transport layers using pulsed laser deposition (PLD) at UVEG, with a laser fluence of 1.5–1.6 J cm^{-2} at 25 Hz and chamber pressures around 10^{-3} mbar. The oxygen partial pressures were controlled by varying the O_2/Ar gas mix, testing four conditions: three at 5.0 x 10^{-3} mbar with increasing O_2 content (40%, 70%, and 100%) and one at 8.0 x 10^{-3} mbar with 100% O_2. Films with 20 nm thickness were grown at a rate of 120 nm per hour, then annealed at 150°C for 30 minutes to enhance conductivity, showing better performance when annealed.
XPS confirmed the 4+ oxidation state of Sn and empirical formulas from $SnO_{1.95}$ to $SnO_{1.83}$ corresponding to 100% and 40% O_2 concentrations, respectively (Figure 53A). The films had high transmittance (~90%) in the visible and near-infrared spectrum with an optical bandgap of ~3.90 eV; small bands from subgap states could also be observed for increasing oxygen vacancies (Figure 53B). Unfortunately, sheet resistance measurements exceeded the detection limit of our tool (>10^6 Ω/□), consistent with high resistance in undoped oxide semiconductors. Finally, AFM revealed very flat surfaces with RMS as low as 1.2 nm (Figure 53C).

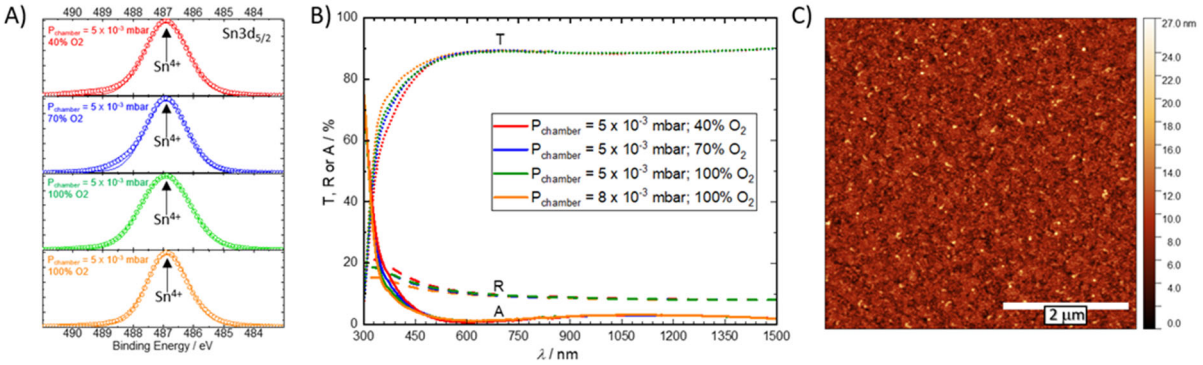

Figure 53 A) XPS, B) transmittance, reflectance and absorptance spectra of SnOx films deposited by PLD at different oxygen partial pressures, and C) AFM image of the optimal PLD-SnOx film.

1.8.2. SnO_2 deposited with atomic layer deposition

SnO_x electron transport layers were also fabricated at UVEG using atomic layer deposition (ALD) with a low-temperature protocol designed to be compatible with thermally sensitive organic and perovskite substrates in p-i-n device configurations. The deposition process involved consecutive purges of tetrakis(dimethylamino)tin vapor for 160 ms and water vapor for 40 ms, each followed by nitrogen purges lasting 30 and 45 seconds, respectively. Repeating this cycle 300 times produced films approximately 20 nm thick.
These films demonstrated a transmittance of around 88% in the 600-1200 nm range, with reduced transmittance between 300 and 600 nm due to reflectance losses and substrate absorptance (Figure 54A). AFM revealed that the films were homogeneous and flat, with a root-mean-square roughness of 0.7 nm (Figure 54C). XPS confirmed the presence of Sn in the 4+ oxidation state and indicated very low carbon contamination, resulting in an empirical formula of $SnO_{1.44}$ (Figure 54B). While higher deposition temperatures could produce stoichiometric and more crystalline films, the chosen low-temperature process helps protect sensitive layers. In p-i-n structures, these SnO_x films not only function as ETLs but also serve as buffer layers for depositing top contacts under harsh conditions and as encapsulants that enhance the stability of thermally unstable materials. For instance, MAPI films remained visually unchanged and kept its crystallinity after 5 hours of heating at 150°C, a condition that would otherwise decompose the perovskite layer (Figure 54D).

Funded by the European Union
This project has received funding from the European Union's Horizon Europe research and innovation programme under grant agreement No. 101082176

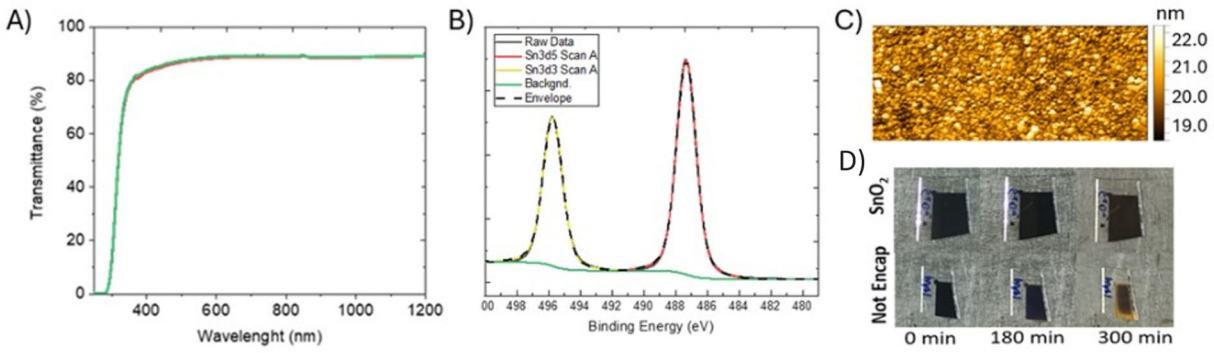

Figure 54: A) Transmittance and B) XPS spectra and C) AFM image of the optimal ALD-SnOx film. D) Test of stability of a glass/MAPI/SnOx stack on a hot plate at 150 oC over time.

1.8.1. Aluminum Zinc Oxide (AZO) developed using pulsed laser deposition

Indium tin oxide (ITO) is currently the dominant material used as a transparent electrode in both display technologies and photovoltaic (PV) applications. Given the rapid growth of these markets and the finite availability of indium, there is an urgent need to identify and develop alternative transparent conductive oxides (TCOs).

At UVEG, an industrial-scale pulsed laser deposition (PLD) process was developed to fabricate AZO films. A laser fluence of 1.5–1.6 J cm^{-2} at 25 Hz and chamber pressures around 10^{-3} mbar were applied. The oxygen partial pressures were controlled by varying the O_2/Ar gas mix. This process is capable of producing highly conductive and transparent AZO layers at room temperature, eliminating the requirement for post-deposition annealing.

The films exhibited exceptionally smooth surfaces, with a root-mean-square (RMS) roughness of only 1.2 nm (Figure 55A). Scanning electron microscopy (SEM) revealed columnar growth (Figure 55B), and X-ray diffraction confirmed a hexagonal wurtzite structure (space group $P6_3mc$, Figure 55C). The films demonstrated high optical transparency, achieving transmittance values exceeding 90% across the 400–1000 nm wavelength range (Figure 55D). Additionally, they maintained low sheet resistances of approximately 25–55 Ω, which remained stable even after several days of exposure to harsh thermal conditions (Figure 55E).

These results have been published at: https://advanced.onlinelibrary.wiley.com/doi/full/10.1002/adfm.202418069

Funded by the European Union

This project has received funding from the European Union's Horizon Europe research and innovation programme under grant agreement No. 101082176

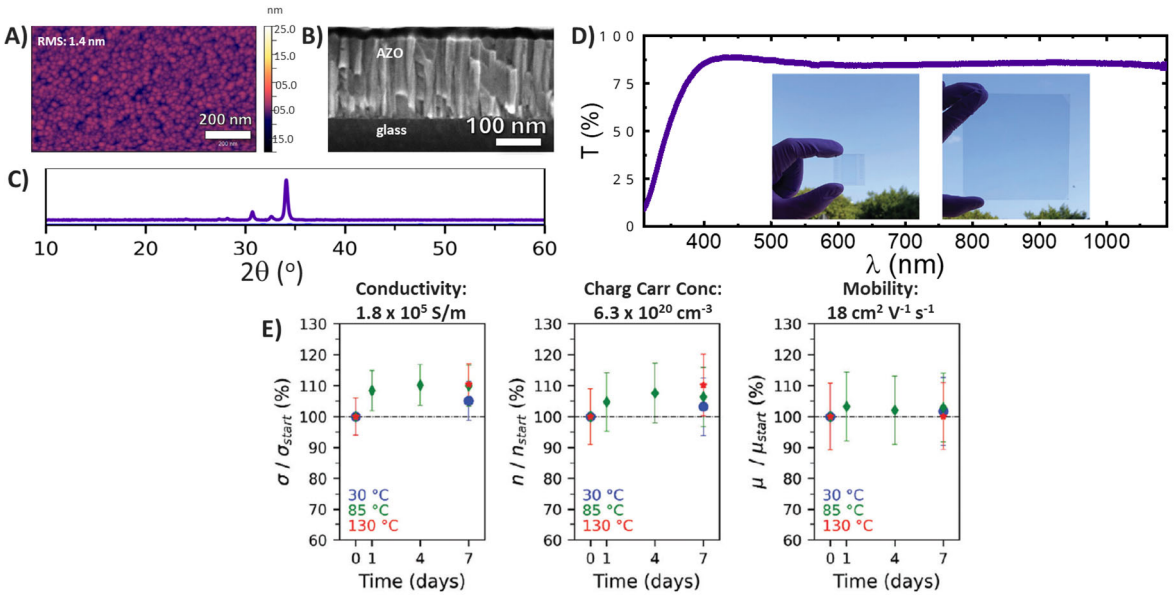

Figure 55: (A) AFM image, (B) SEM cross-section image, (C) XRD spectrum, (D) UV-visible transmittance, and (E) conductivity, charge carrier concentration and electron mobility during ageing of ITO thin films.

4 Conclusions

In conclusion, we have reported here a set of active materials which include perovskite absorbers, charge extracting layers and electrodes. These are the materials selected in terms of optoelectronic properties, stability and suitable processing methods according to the main target of the projects

Funded by the European Union

This project has received funding from the European Union's Horizon Europe research and innovation programme under grant agreement No. 101082176

Funded by the European Union

This project has received funding from the European Union's Horizon Europe research and innovation programme under grant agreement No. 101082176

5 References

IEEE style (https://ieeeauthorcenter.ieee.org/wp-content/uploads/IEEE-Reference-Guide.pdf) example:

[1] T. P. White, N. N. Lal and K. R. Catchpole, "Tandem Solar Cells Based on High-Efficiency c-Si Bottom Cells: Top Cell Requirements for >30% Efficiency," in *IEEE Journal of Photovoltaics*, vol. 4, no. 1, pp. 208-214, Jan. 2014, doi: 10.1109/JPHOTOV.2013.2283342.

[1] M. A. Jameel *et al.*, "Naphthalene diimide-based electron transport materials for perovskite solar cells" in *J. Mater. Chem. A*. Vol. 9, p. 27170-27192, 2021, doi: 10.1039/D1TA08424K

[2] L. Li *et al.*, "Self-assembled naphthalimide derivatives as an efficient and low-cost electron extraction layer for n-i-p perovskite solar cells", *Chem. Commun*. Vol. 55, p. 13239-13242, 2019, doi: 10.1039/C9CC06345E.

Nessuna fonte nel documento corrente.

Funded by the European Union

This project has received funding from the European Union's Horizon Europe research and innovation programme under grant agreement No. 101082176